Hydrothermal regeneration of ammonium as a basin-scale driver of primary productivity

E. E. Stüeken[1,*], K. Kirsimäe[2], A. Lepland[2,3,4], A. R. Prave[1]

1. School of Earth and Environmental Sciences, University of St Andrews, St Andrews KY16 9TS, Scotland, United Kingdom
2. Department of Geology, University of Tartu, 50411 Tartu, Estonia
3. Geological Survey of Norway, 7491 Trondheim, Norway
4. Institute of Geology, Tallinn University of Technology, 19086 Tallinn, Estonia
* ees4@st-andrews.ac.uk

Abstract

Hydrothermal vents are important targets in the search for life on other planets due to their potential to generate key catalytic surfaces and organic compounds for biogenesis. Less well studied, however, is the role of hydrothermal circulation in maintaining a biosphere beyond its origin. Here we explored this question with analyses of organic carbon, nitrogen abundances, and isotopic ratios from the Paleoproterozoic Zaonega Formation (2.0 Ga), NW Russia, which is composed of interbedded sedimentary and mafic igneous rocks. Previous studies have documented mobilization of hydrocarbons, likely associated with magmatic intrusions into unconsolidated sediments. The igneous bodies are extensively hydrothermally altered. Our data reveal strong nitrogen enrichments of up to 0.6 wt.% in these altered igneous rocks, suggesting that the hydrothermal fluids carried ammonium concentrations in the millimolar range, which is consistent with some modern hydrothermal vents. Further, large isotopic offsets of approximately 10 ‰ between organic-bound and silicate-bound nitrogen are most parsimoniously explained by partial biological uptake of ammonium from the vent fluid. Our results, therefore, show that hydrothermal activity in ancient marine basins could provide a locally high flux of recycled nitrogen. Hydrothermal nutrient recycling may thus be an important mechanism for maintaining a large biosphere on anoxic worlds.

1. Introduction

Earth is the only inhabited planet we know of, but it is not the only body in the solar system that is (or was) volcanically active with liquid water in direct contact with fresh volcanic rock. Over the past few decades, the Mars Reconnaissance Orbiter and several rover missions have identified serpentine, phyllosilicates, and silica deposits on Mars that testify to hydrothermal fluid flow in the distant past (e.g., Ehlmann *et al.*, 2010; Viviano *et al.*, 2013; Yen *et al.*, 2021). The Cassini spacecraft and Earth-bound telescopes have detected evidence of active hydrothermal plumes emanating from Enceladus and Europa, respectively (Waite *et al.*, 2006; Roth *et al.*, 2014; Paganini *et al.*, 2020). These finding are tantalizing because hot springs and deep-marine vents have been associated with prebiotic chemical reactions that may be crucial for an independent origin of life. In particular, the gradients in temperature, pH, redox potential, and water composition that typify these environments, along with numerous catalytic minerals, can lead to the formation of organic compounds (Martin *et al.*, 2008).

Hydrothermal vents thus combine two mantras in Astrobiology: "follow the water" and "follow the energy".

Up to the modern day, hydrothermal vents on Earth harbor diverse ecosystems that are adapted to these unique physicochemical conditions. These ecosystems are sometimes regarded as extremophilic oddities of the biosphere that are only remotely related to the more easily visible organisms on land and at the sea surface that play a prominent role in modern biogeochemical processes. For example, carbon, nitrogen, and oxygen cycles have been dominated by the activities of cyanobacteria, eukaryotic algae, land plants and their symbionts since oxygenic photosynthesis evolved and rose to ecological dominance in the Proterozoic and early Phanerozoic, respectively (Falkowski *et al.*, 2004; Brocks *et al.*, 2017; Sánchez-Baracaldo *et al.*, 2021). However, this view does not apply to early Earth or other planetary bodies where oxygenic photosynthesis has not (yet) evolved, land masses are rare or absent, and the flux of nutrients from weathering of the continents is greatly reduced. For such alien, yet potentially habitable worlds, it is imperative to develop a better understanding of how volcanic and hydrothermal processes could supply and recycle nutrients. In other words, hydrothermal vents may well be cradles of life, but their ability to sustain and maintain a diverse biosphere also needs to be elucidated.

Previous studies have shown that vent fluids today can disperse significant amounts of bioavailable iron and copper (Sander & Koschinsky, 2011; Schine *et al.*, 2021) into the open ocean, and they may also have played a role in elevating marine cobalt (Swanner *et al.*, 2014), copper (Stüeken, 2020), nickel (Konhauser *et al.*, 2015), and phosphorus levels (Rasmussen *et al.*, 2021) in the Archean (> 2.5 billion years ago, Ga). Furthermore, N_2 and lightning-derived nitrite may be converted abiotically to ammonium in hydrothermal settings (Brandes *et al.*, 1998; Brandes *et al.*, 2008; Smirnov *et al.*, 2008), which has prompted hypotheses about the origin of biological N_2 fixation in these environments (Preiner *et al.*, 2018). Lastly, and most noteworthy for this study, hydrothermal activity can mobilize ammonium from organic-rich sediments (Lilley *et al.*, 1993) and thus act as an efficient recycling mechanism of fixed nitrogen. The importance of nutrient recycling is not to be underestimated, considering that more than 99% of the biomass of primary producers in the modern surface ocean is subject to oxidative remineralization in deeper waters (Emerson & Hedges, 1988). This remineralization process maintains the deep-marine nutrient reservoirs, which are eventually re-supplied to the surface ocean by upwelling. On early Earth, when the deep ocean was largely anoxic (Lyons *et al.*, 2014), this oxidative recycling pathway would have been severely suppressed (Kipp & Stüeken, 2017). Anaerobic biomass degradation can release ammonium, as exemplified by anoxic environments (e.g., Boudreau & Canfield, 1988). However, recent data from the Black Sea, a modern anoxic basin, suggest that biomass degradation is reduced by 50% under anoxic conditions compared to oxic settings (Jessen *et al.*, 2017). Computational modeling also suggests high degrees of biomass burial for the Precambrian ocean (Kipp *et al.*, 2021), which indicates that nutrient regeneration would have been less efficient. Thus, post-depositional recycling aided by hydrothermal processes may have been important for sustaining the biosphere on a basinal scale. However, despite previous indications of ammonium recycling and biological utilization from Archean and Proterozoic settings (Stüeken *et al.*, 2021a; Stüeken *et al.*, 2021b), the magnitude of this flux has so far not been quantified.

To test how much bioavailable ammonium can be recycled by hydrothermal fluids, we turned to the Paleoproterozoic Onega Basin in NW Russia (ca. 2.0 Ga, Hannah *et al.*, 2008a). The Zaonega Formation is famously known for unusually high organic matter contents of up to 40% (Melezhik *et al.*, 1999) and syn-sedimentary magmatic activity in the form of lava flows and intrusions into wet sediments (Črne *et al.*, 2013). Previous work has documented hydrocarbon seeps that probably resulted from heating of organic-rich sedimentary strata by magmatic intrusions (Qu *et al.*, 2012; Qu *et al.*, 2020). This package of rocks is ideal for

addressing our research question because (a) it shows evidence of hydrothermal alteration of shallow buried organic matter during deposition of overlying strata and (b) the interspersed hydrothermally altered lava flows and intrusions can act as an archive of ammonium concentrations in the fluids by comparison to N-poor unaltered volcanic rocks. We stress that this basin is extreme in its organic matter content and degree of volcanic activity that goes beyond other, more quiescent, settings. However, these features make the Onega Basin a useful endmember where the effects of hydrothermal circulation on nitrogen cycling can be isolated from background processes.

2. Geological Setting and Materials

The Zaonega Formation comprises a ca. 1500 m thick succession of sedimentary and volcanic rocks in the middle-upper part of the Paleoproterozoic Onega Basin succession at the south-eastern margin of the Fennoscandian Shield. It occurs above the carbonate- and evaporite-dominated Tulomozero Formation, which is characterized by anomalously positive $\delta^{13}C_{carb}$ values of the Lomagundi-Jatuli isotope excursion (Brasier *et al.*, 2011; Prave *et al.*, 2021). The Zaonega succession consists mainly of interbedded sandstones, greywackes, mudstones, and dolostones interlayered with basaltic lava flows and intersected by gabbroic sills (Črne *et al.*, 2014). The latter have pepperitic contacts consistent with intrusion into wet, unconsolidated sediments. The upper part of the Zaonega Formation in particular houses numerous magmatic bodies and is exceptionally rich in organic matter, with total organic carbon (TOC) abundances above 10% in many intervals (Filippov, 1994; Qu *et al.*, 2012).

The depositional age of the Zaonega Formation is broadly constrained between ca. 2050 Ma and 1980 Ma. Organic-rich mudstones from the upper part of the formation have yielded Re-Os ages of 2050 Ma (Hannah *et al.*, 2008b; Bauer *et al.*, 2020), whereas a single zircon crystal from a tuff layer in the lower part of the formation provided a U–Pb age of 1982 ± 4.5 Ma (Martin *et al.*, 2015). Mafic intrusions from below, within, and above the Zaonega Formation yield ages that define a ca. 70-Myr time window: 1976 ± 9 Ma (Puchtel *et al.*, 1998) and 1975.3 ± 2.8 Ma (Martin *et al.*, 2015) from underlying units; 1919 ± 18 Ma (Priyatkina *et al.*, 2014), 1956 ± 5 Ma (Stepanova *et al.*, 2014), and 1961 ± 5.1 Ma (Martin *et al.*, 2015) from within the Formation; and 1980 ± 57 Ma (Puchtel *et al.*, 1998), 1988 ± 34 Ma, 1985 ± 57 Ma, and 1969 ± 18 Ma (Puchtel *et al.*, 1999) from overlying units.

The material used in the study was sampled from drill core 12AB obtained by the Fennoscandian Arctic Russia – Drilling Early Earth Project (FAR-DEEP) and coordinated by the International Continental Scientific Drilling Program (ICDP). This core intersects 504 m of the upper part of the Zaonega Formation and contains three magmatic bodies separated from each other by sedimentary rocks. The magmatic bodies at 484-414 m and 119-55 m (a package of sedimentary rocks at 113-95 m) have pepperitic contacts with extensive contact zone alteration and are interpreted as sills that intrude wet sediments. The magmatic body at 367-315 m contains a few scattered amygdales in the upper part, has a sharp unaltered upper contact to the overlying sedimentary rocks, and is interpreted to represent a lava flow. The magmatic bodies are referred hereafter as lower (484-414 m), middle (367-315 m), and upper (119-55 m; note that this consists of two separate sills). We selected samples from core 12AB with particular focus on the hydrothermally altered magmatic bodies to assess the effects of hydrothermal fluid flow on nutrient mobility.

3. Methods

The outer ~0.5 cm of all core samples was cut off with a water-cooled rock saw, and the interiors were hammered into 2-5 mm-sized chips with a steel pestle on a steel plate. The chips were placed into an acid-washed and muffled (500 °C) glass beaker and cleaned by swirling them for 10-20 seconds in DI-water (18 MΩ/cm), methanol, DI-water, 1M HCl (reagent grade), and again DI-water. The rinsed chips were dried in a closed oven at 70 °C overnight and then pulverized with an agate ball mill. Muffled silica sand was run through the mill in between samples. Analyses of this sand showed total N concentrations of less than 1.5 µg/g. The powder was stored in muffled scintillation vials.

For organic carbon and nitrogen isotope analyses, roughly 0.5 g of powder was weighed into a muffled glass centrifuge tube and mixed with 10 ml of 2M HCl using a clean glass rod. The tubes were capped loosely to allow CO_2 gas to escape and placed into an acid-proof oven at 70 °C overnight. The next day, the acid was decanted after centrifugation. Complete dissolution of all carbonate was ensured by adding a few drops of fresh acid at room temperature and monitoring effervescence. The acid was then washed out with 20 ml of DI-water in three iterations such that the residual washed sample was pH-neutral. The decarbonated powder was dried in the oven and then transferred into muffled scintillation vials. For the analyses, aliquots of powder were weighed into tin capsules (8 x 5 mm, Thermo Fisher) and analyzed by flash-combustion in an EA IsoLink with a ramped GC oven coupled via a Conflo IV to a MAT253 IRMS (Thermo Finnigan) (Stüeken et $al.$, 2020). The EA was equipped with a dual-reactor setup with Cr_2O_3 at 1020 °C in the combustion reactor and Cu wire at 650 °C in the reduction reactor. Water vapor was trapped with a magnesium perchlorate column at room temperature. For samples with C/N ratios above c. 120, the analyses were repeated with an additional CO_2 trap packed with soda lime. The He flow in the EA was set to 180 ml/min for the first 110 seconds (valve V2 open) and then lowered to 50 ml/min (valve V2 closed) for the rest of the run. The GC oven was ramped from 35 °C to 240 °C after the elution of the N_2 peak to improve the elution of CO_2. Empty tin capsules were analyzed in each run, and their signal was subtracted from all samples and standards. The measurements were calibrated with the reference materials USGS-40 and USGS-41 and expressed in delta notation as $\delta^{15}N_{bulk} = ([^{15}N/^{14}N]_{sample}/[^{15}N/^{14}N]_{air} - 1)$ x 1000, and $\delta^{13}C_{org} = ([^{13}C/^{12}C]_{sample}/[^{13}C/^{12}C]_{VPDB} - 1)$ x 1000. A series of USGS-41 with different weights was used to calibrate peak areas for total nitrogen (TN) and total organic carbon (TOC) concentrations. USGS-62 was used for quality control and gave a long-term reproducibility of 0.46 ‰ (2 S.D.) for both $\delta^{15}N_{bulk}$ and $\delta^{13}C_{org}$ and better than 10% relative error for TN and TOC abundances. The measured average values of +20.21 ‰ for $\delta^{15}N_{bulk}$ and -14.96 ‰ for $\delta^{13}C_{org}$ are in good agreement with expected values (+20.17 ± 0.06 ‰ and −14.79 ± 0.04 ‰, respectively, Coplen, 2019). Of the 125 samples, 38 were analyzed in replicates, and their average reproducibility was 1.02 ‰ (2 S.D.) for $\delta^{15}N_{bulk}$, 0.92 ‰ (2 S.D.) for $\delta^{13}C_{org}$, and relative error for TN was 11% and 9% for TOC. For samples with total N peak areas of less than 8 Vs, $\delta^{15}N_{bulk}$ could not be measured reliably (SD > 2 ‰) and is therefore not reported. Our results are supplemented by 47 data from a lower-resolution study of the sedimentary strata in the same drill core by Kump et $al.$ (2011).

For metal abundance measurements, aliquots of untreated powder were sent to Australian Laboratory Services (ALS) in Dublin, Ireland. Samples were analyzed by ICP-MS and ICP-OES, following digestion in HNO_3, HF, $HClO_4$, and HCl (method ME-MS61). Seven samples were analyzed in duplicates, and the average reproducibility (RE) was better than 3 % for major elements and better than 5% for all minor elements. Enrichment factors for Zn and Cu were calculated relative to average oceanic basalt (White & Klein, 2014) and normalized to Al as follows: $EF_{basalt} = ([X]_{measured}/[Al]_{measured})/([X]_{basalt}/[Al]_{basalt})$, where [X] is the concentration of Zn or Cu, respectively. For K, which has been significantly affected by post-depositional metasomatism (see below), the measured abundance was first normalized to the sum of $Al_2O_3 + CaO + Na_2O + K_2O$ and then the ratio calculated of measured K_2O to the initial

K_2O of the assumed source rock. We assumed that the basalt that had only undergone mild alteration (here the interior of the lower mafic body at 412-368 m, Fig. 2a) can be used as a reference point for the mafic bodies and average upper Archean crust (Fedo *et al.*, 1995) for the sedimentary rocks. Lastly, we calculated the provenance index, Psi, following the methodology of Lipp *et al.* (2020; 2021).

4. Results

4.1. Organic carbon and nitrogen

Our results (Table 1) are in good agreement with those of Kump *et al.* (2011), where data overlap (see Figs. 3, 4). The organic carbon isotope data also agree well with measurements by Qu *et al.* (2012). Within the sedimentary horizons, TN broadly increases up-section, roughly concurrently with total K enrichments (Fig. 3). Nitrogen is usually introduced into sediments through biomass burial because it is a major constituent of proteins, DNA, and RNA in cells. However, in several places in these samples the behavior of nitrogen across the core contrasts with TOC as reflected by highly variably C/N ratios:

(1) Between the lower and middle mafic bodies at 414-367 m, TOC decreases, while TN remains roughly constant or perhaps slightly increases. This small increase in TN parallels an increase in $\delta^{15}N_{bulk}$ from 1.8 ‰ to 6.6 ‰.

(2) Above the middle mafic body, TOC decreases by two orders of magnitude from high values up to 11% in mudstones (310-270 m) to 0.1% in the sandstone-rich section at 200-240 m, whereas TN increases by one order of magnitude from a few hundred µg/g in the mudstone to a few thousand µg/g in the sandstone. Both shifts are statistically significant (p < 0.005) and explain the drop in C/N ratios in this interval. $\delta^{15}N_{bulk}$ increases from -1.68 ‰ to 8.10 ‰ across this interval and continues to increase to as high as 9.7 ‰ at 120 m.

(3) Unusually high TOC values of up to 40% occur between 136-156 m, which has previously been interpreted as a fossilized oil spill onto the seafloor (Qu *et al.*, 2012). TN abundances are high in this section but comparable to adjacent beds. In contrast, $\delta^{15}N_{bulk}$ values show a drop of several permil within the oil spill horizon to as low as 2.26 ‰.

(4) Within the mafic bodies, TN is most enriched relative to TOC, that is, C/N ratios are consistently low. In the lower mafic body (482-416 m), which likely represents a post-depositional intrusion (Črne *et al.*, 2013), both elements show enrichments at the top; TN is also enriched at the base. In the middle and upper mafic bodies (368-315 m, 119-113 m, and > 94.5 m), no spatial patterns are evident, but the highest TN abundances are comparable to those of adjacent sedimentary beds, whereas TOC is consistently below the sedimentary values. $\delta^{15}N_{bulk}$ within the lower and middle mafic bodies clusters around a mean of 5.3 ± 1.4 ‰, similar to some of the sedimentary strata in between. Also in the upper mafic bodies, $\delta^{15}N_{bulk}$ values of up to 9.1 ‰ match those of surrounding sedimentary strata.

Within the mafic bodies, TN shows moderate to strong correlations with K/Al ratios (r^2 = 0.3 with p = < 10^{-5} for the lower mafic body at 481-416 m; and r^2 = 0.8 with p = < 10^{-5} for the middle mafic body at 353-323 m, Fig. 5a) and no correlations with TOC (r^2 = 0.1 and 0.0, respectively). Within the sedimentary strata only, TN is moderately correlated with K/Al (r^2 = 0.3, p = 10^{-8}, Fig. 5b). Relative to organic carbon, sedimentary TN shows two populations of data where one group (mostly from below 250 m and above 155 m) shows a strong covariance with TOC, driven by samples with > 15 % TOC, and the second group (mostly from 250-155 m) is uncorrelated (Fig, 5c).

4.2. Metal abundances

All metal abundance data generated in this study are shown in Table 2. In terms of the provenance indicator Psi (Lipp *et al.*, 2020; Lipp *et al.*, 2021), the mafic bodies fall close to the mafic endmember, as expected (Fig. 4). This mafic signature is also consistent with the mineralogy, which is dominated by plagioclase and pyroxene in the least altered interior of the lower mafic body (Fig. 2a). The sedimentary strata up to about 250 m broadly reflect this mafic signature before shifting to more felsic compositions above 250 m, likely reflecting a change in provenance. The lower mafic body (484-414 m) shows strong enrichments in K in its top and bottom relative to the weakly altered interior. This trend parallels a mineralogical shift from plagioclase and moderately altered pyroxene in the interior (Fig. 2a) to highly altered pyroxene and replacement of all plagioclase by phyllosilicates at the top (Fig. 2b). Concurrent with these K-enrichments, Cu is slightly depleted, but Zn remains unchanged or shows subtle change only. The middle mafic body (367-315 m), which also shows highly altered residual pyroxene and complete replacement of plagioclase (Fig. 2c), is variably enriched in K as well as Cu and displays an overall slightly higher average for Zn and P. There are few data for the upper mafic bodies, but these are the most K- and N-rich samples.

5. Discussion

5.1. Hydrothermal alteration and ammonium mobility

The Onega Basin experienced significant hydrothermal fluid flow that strongly altered the mafic bodies (Fig. 2, 4) (Črne *et al.*, 2013; Paiste *et al.*, 2020). The depletion of Cu from the lower intrusive mafic body (484-414 m), without concurrent depletion in Zn, is consistent with a highly saline hydrothermal fluid, such as those associated with sedimentary Cu ore deposits where Cu is mobilized from mafic source rocks by deep sedimentary brines (Hitzman *et al.*, 2010). In the case of the Onega Basin, it is likely that such saline fluids were sourced from underlying evaporites as recovered in the Onega Parametric Core (Blättler *et al.*, 2018). The middle mafic body (367-315 m), which is thought to represent a lava flow, is enriched in Cu and slightly enriched in Zn. The relative timing between the lava flow and the lower intrusive body is unknown. However, given the lack of Zn depletion in the intrusion (lower mafic body), a plausible source for these elements in the lava (middle mafic body) are the encasing sediments. In other words, hydrothermal fluids likely mobilized Cu, Zn, and other elements from the sedimentary strata and at least in part deposited them within the lava flow as it underwent alteration.

In the lower mafic body (484-414 m), K is enriched in the same intervals that show Cu depletion. This K-enrichment likely reflects the formation of K-feldspar and sericite, which is a typical alteration phase in hydrothermal settings (Robb, 2005). The K can be derived either directly from seawater (e.g., Brauhart *et al.*, 2001) and/or from the breakdown of K-feldspar initially contained in now K-depleted sediments that sit above or below the mafic body (e.g., Fedo *et al.*, 1995). The strong correlation between K and TN in the altered mafic rocks and the high TN concentrations compared to typical values of a few µg/g in unaltered basalts (Johnson & Goldblatt, 2015) indicate that this K-rich fluid was also enriched in ammonium (NH_4^+). Ammonium and K^+ have the same charge and a similar ionic radius, and therefore they can substitute for one another in mineral lattices (Busigny & Bebout, 2013). For the Zaonega Formation, this process of ammonium incorporation into phyllosilicates was previously proposed by Kump *et al.* (2011). The most likely source for the ammonium are the organic-rich sedimentary strata, as exemplified by modern hydrothermal fluids that are typically ammonium-rich if sediments occur along the fluid flow path (Lilley *et al.*, 1993). A similar transfer of material from organic-rich sediments into the altered intrusion (lower mafic body) has been documented for sulfide (Paiste *et al.*, 2020). If the TN contents of all samples along

the core are compared to their respective TOC contents and an assumed C/N ratio of 10 for initial biomass (Godfrey & Glass, 2011), it turns out that the most organic-rich samples have lost N, while the most organic-poor samples have gained it (Fig. 6c and d), which further supports the idea of TN transfer from organic-rich sedimentary strata into altered mafic rocks.

Importantly, the TN-gain is reflected not only in altered mafic rocks but also in some sedimentary strata. Major element systematics (Fig. 7b) indicate that significant parts of the sedimentary horizons have also undergone K-metasomatism, as sedimentary strata above ~250 m show K-enrichments (Fig. 4, 7). Hence, the relatively high TN concentrations above 250 m (Fig. 3), despite variable TOC levels, reveal that fluids enriched in K and ammonium (and possibly other elements such as Cu and Zn) circulated through most of the sedimentary strata and mafic bodies of the basin.

5.2. Quantifying the hydrothermal ammonium load

The TN data from the altered mafic rocks can provide an estimate of the ammonium concentrations of those fluids. When ammonium is incorporated into secondary phyllosilicates, it adsorbs onto the mineral surface and is taken up into the interlayers of the mineral lattices, as observed in modern sedimentary pore waters where ammonium is incorporated into diagenetic illitic clays (Schroeder & McLain, 1998). Boatman & Murray (1982) derived a correlation between the fluid and mineral N content as a result of this process: $N_{clay} = a_{NH4+}/([1/K_{ads}] + a_{NH4+}) \cdot \Gamma \cdot M_N$, where N_{clay} is the amount of adsorbed ammonium in g/g, a_{NH4+} is the activity of ammonium in the fluid (i.e., the molar concentration multiplied by an activity coefficient of 0.57 for seawater), M_N is the molar mass of nitrogen (14.01 g/mol), K_{ads} is an empirically determined adsorption constant (5.1 L/mol for average mud), and Γ is the cation exchange capacity for average clay (0.96 mmol/g). Their formulation successfully reproduces measured concentrations of modern marine settings (Rosenfeld, 1979; van Raaphorst & Malschaert, 1996). Applying their calibration to the TN-rich altered mafic bodies of the Zaonega Formation, we find that dissolved ammonium levels were as high as 50 mM. These high levels are comparable to modern anoxic pore waters in organic-rich sediments and black smoker fluids (Rosenfeld, 1979; Boudreau & Canfield, 1988; Lilley *et al.*, 1993). For comparison, less extreme marine sedimentary pore waters may contain ammonium levels in the sub-mM range (Caetano *et al.*, 1997; Engström *et al.*, 2005). Hence, such high levels are indicative of the degradation of large amounts of biomass. However, these concentrations would have exceeded the levels one would expect to find at the bottom of restricted marine basins as a result of anaerobic biomass degradation in the absence of hydrothermal processes. This is exemplified by the modern Black Sea, where ammonium levels are approximately 0.1 mM and hydrothermal vents are absent (Brewer & Murray, 1973; Konovalov *et al.*, 2006). Hence, the amount of ammonium liberated by maturation of organic matter passing through the oil window and by circulation of hydrothermal fluids in the Onega basin was likely well above those seen in volcanically quiescent settings of that time.

Ammonium incorporation into clays is affected by salinity and pH (Kithome *et al.*, 1999; Hou *et al.*, 2003), where ammonium incorporation decreases with decreasing pH and increasing salinity. Because the hydrothermal fluid in the Onega Basin was more saline and acidic than modern seawater, given the documented presence of evaporites deeper in the stratigraphy (Blättler *et al.*, 2018), we would thus be underestimating the true amount of ammonium in the fluid.

5.3. Bioavailability of fluid-mobile ammonium

To evaluate the significance of these ammonium-rich fluids for the Paleoproterozoic biosphere, a key question concerns the timing of fluid flow relative to sedimentation and biological activity. Two lines of evidence suggest that at least some of the ammonium-rich fluids emanated into the water column of the basin and probably created locally nutrient-replete conditions as follows: (1) The presence of the syn-sedimentary oil spill, which is most prominent at 156-136 m and begins to show sedimentary expressions in the form of tar balls above 170 m (Qu *et al.*, 2012) (Fig. 2d), and (2) the isotopic composition in $\delta^{15}N$ seen in the upper part of the core (Fig. 3, 5).

With regard to point (1), the oil spill interval and bracketing strata contain tar balls that strongly suggest emplacement of the oil on the seafloor, rather than post-depositional emplacement within the sediment pile, and organic carbon isotope data suggest that this oil was derived from organic matter from deeper in the succession (Qu *et al.*, 2012). Oil forms during the maturation of buried biomass, typically as organic-rich sediments are buried to a depth of the "oil window" at the depth >1500 m, where temperatures of > 70 °C lead to the release of hydrocarbon molecules. In organic-rich sediments of the Zaonega Formation, the oil formation and migration was initiated possibly at much shallower burial depths by intrusion of mafic magmatic bodies (Qu *et al.*, 2012). Importantly, the oil window also marks the point where most ammonium is released from degrading organic matter, as indicated by several studies of younger oil source rocks (Williams *et al.*, 1989; Williams & Ferrell, 1991; Williams *et al.*, 1992). It is, therefore, highly likely that the generation of this oil spill also marked the time when large quantities of ammonium were released into warm aqueous fluids that migrated through the sediment package of the Zaonega Formation and seeped into the water column, along with the methane seep (Qu *et al.*, 2012). Evidence of microbial methane uptake (methanotrophy) in the form of low $\delta^{13}C_{org}$ values is most conspicuous from the top of the core, but it is also apparent immediately above and below the oil spill interval, where $\delta^{13}C_{org}$ values are lighter than the oil spill itself, which is consistent with methanotrophy concurrent with ammonium enrichment. The very low $\delta^{13}C_{org}$ values at the top of the core may indicate higher oxidant availability (O_2 or sulfate) that further boosted methanotrophy at that time (see also below).

With regard to point (2): Ammonium release from organic matter by hot fluids and uptake of ammonium into phyllosilicates are not associated with any significant isotopic fractionation (< 1 ‰) (Ader *et al.*, 2006; Boudou *et al.*, 2008; Koehler *et al.*, 2019), yet the measured $\delta^{15}N$ values across the core spread over a range of more than 10 ‰. In a previous study, the least altered organic matter was identified at 400-370 m, beneath the middle igneous body (Qu *et al.*, 2012). Here, $\delta^{15}N$ values fall between 4-6 ‰, which is similar to the overlying middle mafic body. Since hydrothermal mobilization and uptake of ammonium into clays does not significantly fractionate $\delta^{15}N$ (Ader *et al.*, 2006; Boudou *et al.*, 2008; Koehler *et al.*, 2019), it seems plausible that ammonium with an isotopic composition of 4-6 ‰ was mobilized from biomass in the 400-370 m interval and transferred into the overlying middle mafic body by hydrothermal fluids without any modification of the $\delta^{15}N$ value. Within the middle mafic body at 367-315 m, $\delta^{15}N$ is fairly homogeneous, which also suggests the absence of any significant fractionation during the transfer of ammonium from the underlying sediments into this altered lava flow.

In contrast, the highly altered organic matter above the middle mafic body at 315-270 m is isotopically light in $\delta^{15}N$, as low as -1.7 ‰. The high C/N ratios of these rocks suggest that they are dominated by organic-bound N with relatively little secondary N-enrichment in clays. A scatter plot of $\delta^{15}N$ versus C/N ratios indicates a tendency that the lowest $\delta^{15}N$ values near 0 ± 2 ‰ occur in the samples with the highest C/N ratios (Fig. 5d), which are the most N-depleted, organic-rich sedimentary rocks, particularly at 315-270 m depth. The highest $\delta^{15}N$ values (8-10 ‰) occur within sedimentary rocks immediately above and below the oil spill

(155-135 m), which itself falls between 2-5 ‰. Hence, it appears that, to first order, the altered sedimentary rocks from 315-120 m and above are composed of two nitrogen endmembers: an isotopically light endmember with high C/N ratios (*i.e.*, organic-bound N) and an isotopically heavy endmember with low C/N ratios (*i.e.*, TN-enriched phyllosilicates). Using the kerogen isolate data from Kump *et al.* (2011) for this part of the core as a proxy for the organic endmember, one can calculate the isotopic offset between the organic-bound and silicate-bound fraction to be between 3-10 ‰ with some outliers up to almost 20 ‰ (Fig. 6).

It might be argued that this divergence is explicable due to regional metamorphism. Previous work on metasedimentary rocks of various grades revealed an increasing divergence between kerogen and associated silicates from prehnite-pumpellyite to amphibolite facies (Stüeken *et al.*, 2017; Kipp *et al.*, 2018). For the rocks of the Zaonega Formation, which have undergone regional metamorphism up to lower greenschist facies, an isotopic difference of around 2-4 ‰ between the two nitrogen phases can be expected. The reason for this metamorphism-driven isotope offset is likely related to differing bond strengths between the organic and inorganic nitrogen reservoirs in metasedimentary rocks. However, in the case of the Zaonega Formation, the isotopic difference between kerogen and silicates is, on average, larger than expected, and the two nitrogen phases are spatially well separated by many meters, as suggested by the large variability of C/N ratios across the core (Fig 3). A good illustration of this spatial separation is the interval around the syn-sedimentary oil spill, where the N-depleted oil spill itself is isotopically lighter than the N-enriched bracketing sediments, which indicates that the isotopic divergence pre-dates regional metamorphism. It thus appears that, in this part of the section, the hydrothermally mobilized ammonium was isotopically fractionated after being released from organic matter and prior to incorporation into phyllosilicates.

In modern low-temperature (< 50 °C) hydrothermal fluids from the Juan de Fuca Ridge, Bourbonnais *et al.* (2012) described $\delta^{15}N$ values of up to 12 ‰ in dissolved ammonium. Those values were up to 8 ‰ higher compared to background sediments and high-temperature fluids. They concluded that this isotopic enrichment in ^{15}N in the dissolved ammonium had been imparted by partial biological ammonium uptake or by partial biological oxidation of ammonium to nitrite and nitrate (nitrification). In the former case, the complementary isotopically light phase would have been homogenized with other biomass. In the case of nitrification, the isotopically light nitrogen would be the resulting nitrate vented into the open ocean. From the hydrothermally active Guaymas Basin, Campbell *et al.* (2013) documented a high abundance of anaerobic ammonium oxidizers (ANAMMOX) near diffuse vents, which could also contribute to this isotopic effect. We propose that the large $\delta^{15}N$ range observed in the upper part of our core through the Zaonega Formation reflects similar biological processes. The calculated $\delta^{15}N$ values for the silicate phase of 3-10 ‰ and occasionally up to 20 ‰ (Fig. 6) is likely reflective of the dissolved ammonium in the hydrothermal fluid. Such ^{15}N-enriched values compared to associated organic-bound N are not consistent with known abiotic processes such as hydrothermal ammonium mobilization (Ader *et al.*, 2006; Boudou *et al.*, 2008), clay intake (Koehler *et al.*, 2019), or regional metamorphism (Stüeken *et al.*, 2017; Kipp *et al.*, 2018), but are consistent with biological metabolisms acting on the dissolved ammonium pool. For example, partial biological uptake of ammonium is associated with a fractionation of up to 27 ‰ (Hoch *et al.*, 1992), which could explain both the ^{15}N-enrichment in residual ammonium and the ^{15}N depletion in organic matter. Alternatively, nitrification (fractionation of 14-38 ‰ from NH_4^+ to NO_2^-) (Casciotti, 2009) could have generated ^{15}N-enriched ammonium and a ^{15}N-depleted nitrite (and nitrate) pool that was assimilated elsewhere. The latter interpretation would be in line with that of Kump *et al.* (2011), who also interpreted the progressive increase in $\delta^{15}N$ up section as evidence of increasingly oxic conditions, and it would be consistent with anomalously low $\delta^{13}C_{org}$ at the top of the core that has been interpreted as evidence of methanotrophy (Qu *et al.*, 2012). Although the nitrogen data alone

do not allow for distinction between ammonium assimilation and nitrification, the latter is perhaps favorable in light of the carbon isotope data. In fact, the inferred bioavailability of ammonium in the upper half of the core, coinciding with a progressive depletion in $\delta^{13}C_{org}$ values (Fig. 1), indicates that ammonium was biologically metabolized in parallel with methane in the Onega basin, and both substrates were likely provided by volcanic and hydrothermal activity. In other words, local hydrothermal activity created not only methane-rich but also ammonium-rich conditions by recycling this nutrient from older buried biomass.

6. Conclusions

In summary, our data from the Paleoproterozoic Onega Basin in NW Russia show strong evidence of hydrothermal ammonium remobilization from organic-rich sedimentary strata concurrent with previously inferred mobilization of hydrocarbons, including methane. Mafic intrusions provided a heat source that took organic matter through the oil window and initiated ammonium release into fluids. Further evidence for such ammonium-rich fluids comes from pervasive K-metasomatism in the hydrothermally altered mafic rocks and in the upper sediment package of the core. The ammonium that was liberated by this process likely reached concentrations of several millimole per liter, as indicated by the high N-enrichments in the altered mafic rocks. Such high concentrations are consistent with modern pore waters, but they exceed the concentrations found in volcanically quiescent anoxic basins like the Black Sea. This finding highlights the ability of hydrothermal activity to drive ammonium mobilization at a large scale in the Paleoproterozoic Onega basin. Furthermore, the isotopic divergence between silicate-bound and kerogen-bound nitrogen in these rocks is most parsimoniously explained by biological fractionation imparted on the dissolved ammonium reservoir of the hydrothermal fluid. In other words, we see evidence that the hydrothermal ammonium was bioavailable and created locally N-replete conditions. It is conceivable that this nutrient enrichment enhanced biological productivity and biomass production, which may have resulted in positive feedback on the ammonium recycling flux.

In the modern ocean, where most nutrients are recycled by oxidative degradation of biomass in the oxic water column, hydrothermal nutrient sources are minor on a global scale. However, in the Precambrian, when the deep ocean was anoxic, this hydrothermal recycling mechanism could have locally offset the absence of water column recycling and created nutrient-rich refugia for microorganisms. In fact, we speculate that isotopic offsets between kerogen and silicates that have previously been documented from other succession may at least in part also reflect biological activity (Godfrey *et al.*, 2013; Stüeken *et al.*, 2017; Kipp *et al.*, 2018). Evaluating this possibility will require more detailed investigation of each setting. In any case, it is likely that similar processes would occur on other planetary bodies where hot fluids interact with buried biomass. Thus, hydrothermally active basins are not only ideal sites for an independent genesis but perhaps also for the sustenance of a diverse biosphere.

Conflict of Interest: The authors have no conflicts of interest to declare.

Table 1: Organic carbon and total nitrogen data generated in this study.

Depth [m]	TN [ppm]	$\delta^{15}N_{bulk}$ [‰]	TOC [ppm]	$\delta^{13}C_{org}$ [‰]
92.93	478	8.36	603	-36.05
93.29	1912	4.64	1150	
94.53	1439	7.78	4611	-41.46
94.85	3063	7.35	45113	-38.63
96.01	2230	5.00	205059	-39.26
100.27	581	0.90	84993	-37.32
103.73	2413	5.68	200427	-39.89
112.07	2649	3.68	315517	-40.42
113.02	370	2.96	51941	-39.89
113.09	1348	6.96	1533	-38.28
114.45	116	0.48	18378	-36.77
116.34	4025	8.32	877	-32.92
118.07	6168	9.06	123	-38.26
119.33	6933	9.71	266	-32.48
119.38	3626	9.81	23954	-34.60
119.75	1430	4.24	150004	-32.51
121.45	45	7.82	1112	-26.11
124.6	1256	6.68	71504	-31.42
127.01	22		2553	-24.47
131.64	1948	8.61	10091	-29.93
132.86	2641	5.26	332839	-30.01
135.5	2873	9.73	5693	-27.56
137.9	3638	2.90	378895	-26.34
138.42	3522	2.26	396363	-26.24
138.55	3259	5.32	278864	-26.39
142.35	3842	3.25	445891	-25.66
144.83	3317	3.95	383645	-25.41
152.8	3978	3.13	456323	-25.62
153.37	2120	8.23	94424	-28.92
154.58	3530	3.04	423031	-25.75
156.24	453	4.06	49630	-28.36
156.9	1864	7.50	53077	-28.66
164.03	4902	8.24	43865	-29.43
167.11	3657	8.47	58745	-28.25
168.17	2888	8.40	95805	-28.34
173.46	2055	8.51	91381	-29.34
181	2536	8.58	51978	-27.90
202.21	1449	5.28	94482	-26.90
202.88	3672	6.62	2424	-26.26
204.84	1226	4.19	223565	-27.81
207.44	1444	5.67	7265	-25.05
209.14	932	4.55	29304	-26.05
211.8	497	5.69	6345	-25.14

214.08	454	5.14	10832	-23.83
226.64	89	1.56	10558	-18.46
229.83	2442	5.10	11832	-18.17
236.58	3019	5.43	1140	-18.24
240.02	1566	5.75	2853	-20.94
245.73	926	7.33	38588	-20.49
250.75	1999	2.94	241433	-24.29
254.83	1672	7.07	90223	-23.60
270.11	356	0.81	48399	
286.12	344	0.33	47227	-24.90
302.4	307		48953	-25.94
304.79	208	-1.68	45855	-24.48
308.19	544	-0.01	81203	
311.77	294		48821	-26.30
315.59	119	4.84	411	-24.76
316.8	789	6.09	242	-26.47
319.22	665		101829	-26.56
320.53	732	5.22	51	-31.38
323.19	3583	5.91	440	-26.88
324.72	1345	5.47	372	-29.78
326.14	215	5.27	371	-28.24
327.88	12		1863	-26.36
330	4		128	-28.31
330.86	101		20851	-27.51
331.5	120		28853	-27.39
332.16	17		4950	-27.20
332.17	3		169	-29.07
332.58	8		114	-29.79
333.15	135	4.10	77	-30.31
333.78	1663	5.65	99	-32.76
334.62	1335	5.79	68	
336	347	5.41	144	-34.82
339.41	1323	5.70	1937	-27.61
341.23	694	5.54	667	-27.67
343.72	226	5.81	138	-30.60
344.32	79	8.56	2460	-27.44
345.25	87	4.16	580	-27.43
346.32	34	5.37	31	-27.00
348.88	410	5.24	512	-27.66
350.3	643	5.58	98	-30.86
351.04	504	5.39	147	-29.35
352.1	252	5.30	13	-29.79
353.63	672	5.17	132	-29.98
416.15	34	2.25	727	-22.18
417.44	133	5.46	409	-23.02
418.17	248	5.62	582	-22.99

420.02	30	5.76	112	-24.61
421.48	207	5.19	292	-20.03
423.08	160	5.22	224	-17.04
424.12	200	5.19	194	-16.45
424.63	398	6.45	146	-15.34
425.88	583	6.32	183	-18.41
426.94	190	4.93	446	-16.25
428.22	63	5.20	251	-15.13
429.97	137	4.77	224	-15.89
431.46	32	3.81	247	-14.92
432.9	49	4.26	238	-13.61
434.76	70	4.92	230	-16.06
435.72	92	4.99	272	-16.57
436.8	331	6.77	471	-19.18
439.1	6		98	-24.36
441.16	6		46	-25.61
442.86	5		87	-24.75
446.06	3		68	-26.90
449.29	5		63	-25.94
451.61	4		113	-25.17
453.61	4		74	-26.88
457.6	5		60	-27.74
460.35	15		57	-29.26
462.99	7		97	-28.25
465.25	6		83	-29.01
467.73	6		113	-29.15
469.31	11		46	-30.35
471.6	7		44	-29.46
474.29	6		45	-30.95
476.82	49	3.85	47	
476.86	55	4.13	52	-29.78
479.15	42	4.20	51	-29.44
479.16	31	4.51	58	
480.11	118	4.92	34	-29.66
481.06	163	4.43	54	-29.11
481.72	215	5.32	50	-28.47

Table 2: Metal abundances generated in this study.

Depth [m]	Ag [ppm]	Al [%]	Ca [%]	Co [ppm]	Cu [ppm]	Fe [%]	K [%]	Mg [%]	Mn [ppm]	Mo [ppm]	Na [%]	Nb [ppm]	Ni [ppm]	P [ppm]	Sc [ppm]	Th [ppm]	Ti [%]	U [ppm]	V [ppm]	Zn [ppm]
92.93	0.42	7.1	2.35	39.5	225	8.85	0.92	2.57	900	0.75	2.89	10.2	60.3	1050	43.7	2.55	1.16	0.5	400	106
113.09	0.77	7.39	2.13	19.4	288	5.65	1.5	1.72	340	0.92	3.01	12.6	120.5	1230	46.9	3.42	1.49	0.9	496	28
114.45	0.28	6.3	4.6	38.7	210	9.59	1.08	2.84	1360	0.81	2.12	10.4	58.3	1080	39.1	3.28	1.155	0.6	391	101
116.34	0.24	6.24	5.31	54.4	144	10.25	2.21	2.87	1340	0.62	1.67	8.4	88.3	850	34	2.35	1.135	0.4	376	106
315.59	0.11	6.42	3.58	49.6	426	12.25	0.24	3.74	1230	0.91	1.37	14.8	47	1380	39.9	3.3	1.62	0.6	504	148
316.8	0.12	6.14	2.54	46	363	12.2	1.1	2.47	1330	0.95	1.44	15.3	41.7	1430	37.6	3.44	1.62	0.6	466	140
323.19	0.1	6.1	2.03	49.3	417	13.9	2.41	2.59	1610	0.99	0.96	15.2	36	1250	41.1	2.7	1.855	0.5	563	182
324.73	0.09	6.14	3.12	47.3	318	12.6	2.21	2.57	1500	0.73	0.71	11.7	41.8	980	39	3.33	1.315	0.6	478	161
326.14	0.11	5.97	2.86	57.8	441	12.65	0.37	2.38	1790	1.1	1.39	16.4	25.2	1570	39.2	3.37	1.695	0.6	407	148
327.88	0.22	6.36	2.19	52.7	822	13.35	0.06	2.81	1610	0.85	1.13	13.1	56.2	1160	44.6	2.6	1.855	0.5	670	188
330	0.05	6.12	3.72	35.7	402	8.02	0.05	1.97	923	0.73	2.44	15.4	42.7	1600	36.4	3.44	1.72	0.7	446	118
332.58	0.08	6.12	2.15	43.5	405	13.05	0.03	3.25	1520	0.73	0.8	14.2	41.5	1340	38.9	2.82	1.605	0.5	508	174
333.15	0.09	6.38	2.52	44.6	426	12.95	0.21	2.89	1490	0.69	1.32	15.5	40.6	1490	39.6	3.21	1.8	0.6	522	165
333.78	0.04	6.39	2.57	46.9	402	13.5	1.62	2.8	1550	0.91	1.1	14.9	37	1470	39.3	3.21	1.745	0.6	522	171
336	0.05	5.97	4.4	42.8	259	13.1	1.43	2.04	1910	1.18	1.28	18.5	11.4	1720	35.5	4.1	1.665	0.8	276	176
339.41	0.08	6.19	5.64	53.8	385	13.3	1.33	3.06	1580	0.61	1.19	11.1	61.6	1180	42.7	2.29	1.7	0.4	690	154
341.23	0.06	6.27	6.05	45	147.5	11.5	1	2.59	1230	0.57	0.94	12.5	54.5	880	35.1	4.44	1.435	0.8	586	122
343.72	0.11	5.6	4.95	52.3	473	13.1	0.47	2.87	1780	0.65	1.36	11.3	63.6	950	44.7	2.49	1.77	0.5	746	146
345.25	0.13	6.63	5.39	53.1	691	12.05	0.31	3.16	1390	0.8	2.34	11.7	74.8	1130	41.3	2.45	1.695	0.5	712	143
348.88	0.14	6.67	5.59	50.7	502	12.55	0.82	2.96	1460	0.71	1.81	10.8	74.4	990	39.4	2.26	1.565	0.5	652	140
350.3	0.13	6.58	6.57	50.9	582	12.6	0.79	2.91	1430	0.63	1.31	10.8	72.3	1040	38.4	2.38	1.515	0.5	626	142
351.04	0.1	6.69	6.04	50.7	420	12.15	0.75	2.99	1450	0.69	1.76	11.2	74.1	1020	38.4	2.46	1.54	0.5	626	139
352.1	0.12	6.9	6.73	52.9	469	12.3	0.55	3.13	1450	0.85	1.94	11.5	77.2	1020	40.9	2.62	1.565	0.5	643	143
416.15	0.04	7.69	8.36	35.1	54.7	8.72	0.42	4.04	1650	0.36	1.99	7.9	70.4	530	35	1.63	0.87	0.3	318	104
417.44	0.06	7.71	7.71	49.1	47.7	9	0.7	3.83	1570	0.42	1.68	7.8	89.6	560	33.3	1.6	0.855	0.3	300	118
418.17	0.09	4.9	3.4	55.3	142	10.05	0.78	3.05	1310	0.22	0.79	2.8	143	210	13	0.59	0.353	0.1	157	100
420.02	0.01	7.72	7.89	49.9	37	9.4	0.67	4.03	1560	0.44	1.62	8.1	76	550	36	1.67	0.891	0.3	315	119
421.48	0.04	7.29	6.82	45.7	97.2	9.78	0.81	3.97	1580	0.43	1.93	8.5	75.9	600	34.9	1.7	0.959	0.3	313	121
423.08	0.06	6.54	9.11	48.3	131.5	9.77	0.47	3.55	1530	0.26	1.51	5	73.1	380	22.7	1.05	0.59	0.2	240	124
424.12	0.03	7.89	6.66	47.6	82.7	9.72	0.79	3.85	1460	0.37	1.8	6.8	92	470	31.1	1.37	0.796	0.3	286	121
424.63	0.04	7.63	6.88	47.5	75.3	9.6	0.77	3.93	1530	0.43	1.69	7.8	85.6	540	36.9	1.57	0.91	0.3	334	120

425.88	0.005	8.07	6.35	44.6	13.5	10.5	0.96	4.18	1560	0.43	2.01	7.7	84.3	550	36.7	1.56	0.894	0.3	328	127
426.94	0.02	7.25	6.76	44.7	63.1	10.25	0.61	3.88	1710	0.39	2.52	7.2	72.5	500	35.2	1.4	0.853	0.3	322	137
428.22	0.02	6.88	7.52	48.4	95.5	11.2	0.6	3.55	1670	0.54	1.63	9.9	47.1	670	43.7	2	1.125	0.4	417	163
429.97	0.01	7.17	7.43	41.1	18.1	10.65	0.79	3.2	1390	0.45	1.72	10	48.6	680	45.2	2.07	1.15	0.4	430	144
431.46	0.04	7.14	7.2	49.6	95.7	9.31	0.7	4.06	1410	0.46	2.01	8.5	59.2	530	42.7	1.65	0.987	0.3	360	116
432.9	0.02	6.82	7.78	43.6	46.3	10.3	0.52	3.43	1760	0.5	1.91	9	43.5	610	41.2	1.7	1.105	0.3	406	116
434.76	0.03	7.1	6.04	45.1	47.4	8.42	0.78	3.8	1330	0.32	2.12	5.8	86.7	420	32.9	1.16	0.735	0.2	281	106
435.72	0.02	7.33	6.12	47.7	81.3	9.56	0.74	3.95	1510	0.39	2.18	8.2	79.2	550	35.5	1.61	0.942	0.3	337	119
436.8	0.32	2.85	20.6	84.5	155.5	9.11	0.72	1.26	1190	0.77	0.96	4.9	45.3	390	11.2	0.96	0.53	0.2	166	57
439.1	0.01	7.34	6.55	47.6	61.5	9.62	0.38	4	1510	0.36	2.35	7	86	480	36	1.27	0.895	0.3	326	115
441.16	0.04	7.79	6.54	47.7	85.7	9.15	0.2	4.12	1480	0.37	2.64	7.7	89.6	520	32.9	1.49	0.898	0.3	321	122
442.86	0.02	7.04	6.1	39.3	88	9.95	0.34	3.59	1500	0.62	2.55	9.2	35.7	600	39.8	1.62	1.045	0.3	368	98
446.02	0.04	7.54	6.06	52.1	99.6	8.78	0.24	4.04	1410	0.38	2.48	7.5	102	440	35.2	1.27	0.854	0.3	297	117
449.29	0.03	7.5	6.45	50.5	77.8	8.7	0.26	4.05	1440	0.37	2.23	7.5	98	490	32.4	1.34	0.832	0.3	290	108
451.61	0.02	7.72	5.47	47.7	57.3	9.93	0.28	3.78	1560	0.57	2.66	8.4	97	580	27.1	1.51	0.885	0.3	292	116
453.61	0.03	7.68	6.48	47.8	76.3	8.43	0.21	3.89	1380	0.39	2.41	7.4	98.4	480	29.8	1.26	0.816	0.3	279	108
457.6	0.05	7.79	6.27	49.1	94.5	8.31	0.34	4.06	1320	0.38	2.4	7.5	106.5	490	30.3	1.64	0.722	0.3	267	96
460.35	0.05	7.8	6	49.6	87.6	8.31	0.73	4.01	1330	0.32	2.17	6.4	110.5	460	30.2	1.13	0.774	0.2	272	99
462.99	0.04	7.96	6.09	49.2	73.6	8.57	0.46	4.15	1380	0.37	2.41	7.1	113	420	31.7	1.24	0.809	0.3	287	110
465.25	0.03	7.7	5.24	50.4	54.7	9.63	0.25	4.82	1660	0.32	2.26	6.9	93.8	480	31.2	1.22	0.781	0.2	280	137
467.73	0.02	7.79	5.69	42.1	32	8.51	0.31	4.4	1390	0.32	2.51	7.1	112.5	510	32.1	1.29	0.834	0.3	290	102
469.31	0.04	7.59	5.62	48.2	43.7	8.62	0.3	4.45	1390	0.4	2.53	6.9	118.5	470	32.1	1.23	0.792	0.3	281	93
471.6	0.04	7.47	4.45	39.7	32.8	8.52	0.18	4.66	1380	0.35	2.99	7.6	82.5	500	33.1	1.29	0.853	0.3	281	108
474.29	0.005	7.37	5.73	48.8	20.8	8.19	0.27	4.71	1410	0.4	2.56	7.4	108	500	33.4	1.31	0.861	0.3	293	119
476.82	0.04	7.21	5	57.5	49.4	10.95	0.4	5.77	1790	0.39	2.08	7.7	103.5	480	31.5	1.55	0.804	0.3	272	152
479.15	0.1	7.51	4.69	55.8	147.5	8.55	0.71	4.6	1530	0.41	2.64	7.4	119	500	32.9	1.39	0.83	0.3	289	88
480.11	0.1	7.56	4.71	56.9	81.9	9.27	0.85	4.69	1600	0.42	2.55	8	128.5	510	35.5	1.47	0.872	0.3	305	80
481.06	0.01	7.47	4.4	44.4	20.1	9.11	1.11	4.58	1530	0.41	2.58	7.7	99.4	510	34.2	1.42	0.846	0.3	302	98
481.72	0.03	7.41	3.58	34	33.6	8.24	1.47	4.26	1130	0.44	3	8.6	89.2	560	37.6	1.57	0.935	0.3	310	119
353.63	0.13	6.76	6.28	53.5	573	13.05	0.94	3.03	1600	0.81	1.62	11.2	76.6	1140	38.8	2.54	1.565	0.5	630	153
94.53	0.81	5.44	9.72	45.7	242	8.16	1.21	2.78	978	0.88	1.55	8.3	109.5	740	32.4	2	0.833	0.9	311	42
93.29	0.39	8.59	1.29	23	124.5	6.1	2.41	2.99	443	0.92	1.42	13.2	57.8	1220	54.1	2.8	1.435	0.7	522	110
344.32	0.11	7.13	4.46	41.5	312	12.5	0.39	2.22	2050	0.75	2.27	14.2	51	710	27.7	6.32	1.04	1.2	461	127
332.17	0.05	7.35	2.67	55.6	254	14.35	0.04	4.44	1740	0.24	0.97	7	93.8	570	46.7	1.04	1.04	0.9	438	181
334.62	0.12	6.1	4.4	54.6	508	13.8	1.8	2.51	1960	1.03	0.96	14.5	38.3	1280	38.5	2.87	1.64	0.6	495	173

118.07	0.55	6.4	3.41	49.1	366	11.6	2.93	2.98	1240	0.72	0.52	10	78.7	1030	37.7	2.9	1.27	0.5	419	146
346.32	0.44	5.55	10.1	63.2	3080	12.35	0.13	2.71	1470	0.49	1.11	5.5	91.4	410	21.3	1.14	0.911	0.2	521	188
320.53	0.08	6.69	2.16	43.9	342	12.9	0.67	2.97	1310	0.45	1.37	16	45.9	1450	43.1	3.15	1.79	0.6	552	169
119.38	0.36	2.13	21.5	71.5	328	8.12	1.13	3.48	3000	0.41	0.01	3.5	148	280	12.2	1.9	0.281	0.7	135	62
302.4	0.01	1.13	1.2	4.4	20.8	1.73	0.11	0.82	257	0.08	0.19	0.6	12.3	20	6.8	0.17	0.104	0.1	67	19
311.77	0.01	1.17	0.63	6.9	4.9	1.13	0.05	0.49	168	0.12	0.57	0.7	35.2	30	5.2	0.23	0.102	0.2	51	12
319.22	0.02	6.66	5.36	41.5	111.5	12.45	0.26	5.53	1670	0.44	0.46	3.3	158	560	45.5	0.17	0.606	0.7	316	185
113.02	1.21	1.59	5.64	23.3	703	14.65	0.25	1.85	948	3.63	0.04	4.2	312	170	2.5	2.9	0.146	1.3	45	35
94.85	0.23	4.97	13.95	6.7	15.6	1.3	2.21	0.78	1430	1.88	0.42	6	17	170	10.5	2.34	0.13	1.3	262	1490
96.01	0.55	4.73	0.2	5.5	11.7	1.92	1.55	1.03	114	12.35	1.21	18.6	76.1	230	17.2	8.74	0.32	3.5	267	101
100.27	0.16	0.96	22.9	4.5	73.7	2.13	0.65	2.49	2100	1.99	0.01	1	5.3	1000	1.6	0.94	0.038	0.3	9	23
103.73	2.43	3.62	6.76	79.8	48	8.48	1.55	1.58	656	19.3	0.25	9.9	993	180	7.7	3.21	0.178	3.8	573	384
112.07	1.14	4.78	0.12	7.2	4.7	2.03	1.64	1.34	156	30.6	1.1	12	74.8	300	10.4	9.15	0.408	6.4	478	1300
119.75	0.03	4.53	0.36	4.6	18.9	1.57	0.94	1.94	165	7.4	2.39	12.3	34.3	960	6.5	7.26	0.272	3.8	125	132
121.54	0.07	3.03	17	16.2	37.9	4.24	1.69	4.8	2730	0.44	0.04	5.6	24.9	1070	8.3	4.44	0.207	0.7	39	101
124.6	0.36	6.31	1.32	31.4	50.7	2.85	2.01	1.21	260	2	2.51	17.3	66.9	430	17	10	0.583	3	163	165
127.01	0.07	0.71	18.4	3.7	41.9	6.75	0.51	9.9	5500	1.06	0.01	1.2	11.2	430	1.6	0.85	0.05	0.3	11	28
131.64	0.63	6.43	6.8	38.8	57.6	4.34	2.11	1.23	886	1.49	2.02	13	76	680	36.5	6.56	0.596	1.7	190	73
132.86	2.15	4.42	0.57	61.2	333	6.71	3.09	1.98	153	430	0.28	14.4	276	2150	15.9	9.29	0.297	74.6	909	416
135.5	1.45	7.47	0.08	103	149	11.85	4.33	3.26	266	6.56	0.22	15.3	204	380	42.3	1.25	1.065	2.5	465	104
137.9	0.65	3.71	0.07	24.4	193	3.19	1.93	0.53	60	27.7	0.59	5.2	315	260	14.6	4.8	0.255	12.5	254	79
138.42	0.68	3.23	0.08	20.1	139	1.93	1.68	0.46	60	7.51	0.57	4.1	215	290	11	4.99	0.187	9	178	80
138.55	0.62	5.08	0.1	38.4	118	3.03	2.87	0.89	82	5	0.39	9.1	173	390	14.9	6.21	0.42	9.3	227	116
142.35	0.11	0.62	0.02	4.3	29.5	0.54	0.35	0.11	14	2.13	0.07	1	86.6	60	2.2	1.24	0.046	2.6	47	239
144.83	0.51	2.48	0.05	18.7	129.5	1.86	1.47	0.42	66	8.05	0.25	3.8	311	200	7.7	4.2	0.16	10.3	190	358
152.8	0.55	2.95	0.05	19.9	197	1.99	1.62	0.49	53	9.34	0.33	4.9	360	210	9.6	5.23	0.197	12	211	145
153.37	1.35	6.89	0.16	59.2	239	8.81	3.8	1.97	155	7.54	1.08	13.2	135	660	27.1	7.82	0.629	3.9	283	223
154.58	0.5	3.24	0.06	20.1	153	2.06	1.72	0.54	50	9.18	0.19	4.9	384	220	9.9	5.05	0.201	12.1	217	154
156.24	0.18	2.18	13.2	12.4	30.7	4.09	1.38	3.83	1020	2.68	0.03	2	54.2	160	8.8	1.09	0.131	3	78	5900
156.9	0.31	8.77	0.16	27.1	14.9	5.23	3.32	9.61	206	2.18	0.37	19.1	87.6	670	22	9.57	0.73	2.8	192	153
164.03	0.3	10.05	0.07	12.7	37.1	2.42	4.04	2	43	7.23	0.03	39.8	51.5	240	25.6	32	0.691	8.5	320	167
167.11	0.42	9.12	2.46	18	40.3	2.45	4.77	1.99	201	17.9	0.1	136.5	79.6	370	25.9	31	0.83	13.1	371	515
168.17	0.46	7.54	2.03	16.9	101	2.18	4.27	2.07	166	18.75	0.31	28.6	83.8	570	19.7	20.4	0.565	10.7	416	159
173.46	3.76	5.73	0.38	117.5	870	14.85	3.32	2.44	96	50.9	0.3	23.1	698	590	28	5.01	0.833	6.9	566	224
181	0.36	6.73	0.2	10.4	443	5.1	3.37	1.53	68	21.9	0.41	120.5	75.5	390	17.4	25	0.364	6.8	304	472

|																				
202.21	0.05	4.98	0.77	22.1	19.4	3.71	1.99	2.31	196	6.64	0.44	1.9	63.4	320	35	1.26	0.266	1.1	255	110
202.88	0.04	9.21	0.26	27.5	13.1	4.73	4.67	3.17	176	1.73	0.34	4.2	76.6	920	48.2	0.25	0.749	1.7	473	80
204.84	0.01	0.21	19.6	2.3	5.5	4.7	0.08	9.86	2150	1.73	0.01	0.1	3	110	1.9	0.11	0.013	0.1	26	15
209.14	0.18	7.6	0.54	41	177	10.7	3.08	4.56	322	0.23	1.04	4.1	142	200	45.3	0.48	0.639	1.4	327	135
211.8	0.19	7.74	0.08	47.6	169	9.71	3.02	3.47	202	0.21	1.96	4.2	110	290	43.8	1.23	0.623	0.8	290	436
214.08	0.24	8.21	0.04	37.3	231	10.65	2.93	3.5	161	0.14	2.45	10.4	103.5	170	46.9	0.67	0.683	1	302	109
226.64	0.02	3.73	7.13	27.7	65.1	6.56	0.69	6.22	1240	0.025	0.59	2.1	45.3	680	25.9	1.44	0.234	0.2	123	47
229.83	0.005	9.64	0.07	17.3	66.7	6.87	4.12	2.85	209	0.05	1.74	4.1	41.1	270	57	0.26	0.736	0.3	291	47
236.58	0.005	9.89	0.06	4.3	4.5	4.33	4.84	3.9	113	0.2	1.38	4.7	16	40	55.2	0.28	0.598	0.4	419	132
240.02	0.01	7.01	0.55	9.6	22.3	2.15	3.34	3.79	53	0.14	1.58	3.1	70.5	1800	38	0.36	0.566	0.2	243	78
245.73	0.22	6.74	0.06	12.8	53.8	2.66	2.74	1.52	49	0.13	2.86	6.3	106.5	150	34.5	4.03	0.403	0.7	116	152
254.33	0.29	2.59	22.6	14.3	180	2.8	1.93	1.1	791	13.35	0.51	1.9	162	140	12.4	0.96	0.185	2.8	170	124
270.11	0.03	6.01	3.66	46.7	114.5	8.49	1.71	2.28	620	0.93	2.64	3.9	103.5	230	38.6	0.49	0.669	0.8	329	48
286.12	0.08	6.83	1.4	110.5	770	11.25	1	4.41	683	2.08	1.8	6.1	148.5	420	40.9	0.73	0.686	1	307	174
304.79	0.02	2.33	0.25	5.6	102.5	3.26	0.02	1.77	343	0.09	0.44	1.2	16.2	80	13.3	0.17	0.202	0.1	100	40
308.19	0.01	1.15	0.7	4.7	6	1.15	0.08	0.51	170	4.28	0.53	0.7	46.8	60	5	0.72	0.071	1	55	12
332.16	0.11	6.5	2.97	47.4	473	12	0.02	3.35	1440	0.53	1.31	13.7	57.8	1290	38.8	2.93	1.56	0.6	508	169
119.33	0.05	5.51	6.42	26	123	7.9	2.96	6.34	1330	0.67	0.35	8.3	58.3	1000	32.5	2.66	1.06	0.5	376	138
330.86	0.03	9.35	1.12	71.7	51.7	15.65	0.06	5.17	1750	0.52	2.14	5	241	520	44.1	0.35	0.922	1.5	461	203
331.5	0.04	4.74	0.94	42.7	212	6.54	0.05	2.21	788	17.35	1.49	2.6	152.5	180	23.1	0.53	0.406	0.9	251	149

Figures
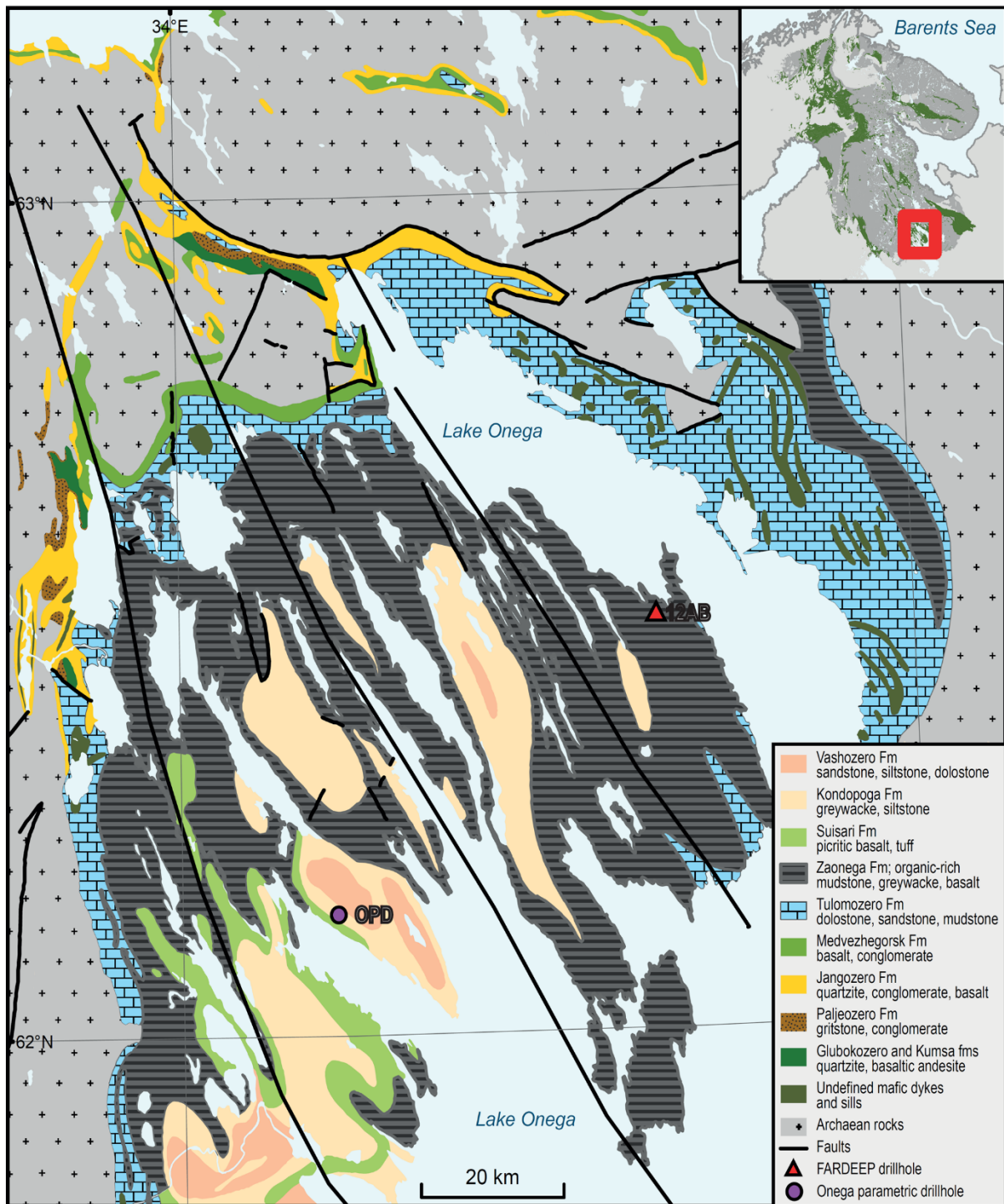
Figure 1: Simplified geological map of the Onega Basin, NW Russia. Red triangle = location of drill hole 12AB used in this study. OPD is the location of the Onega Parametric Drill core (modified after Koistinen *et al.*, 2001).
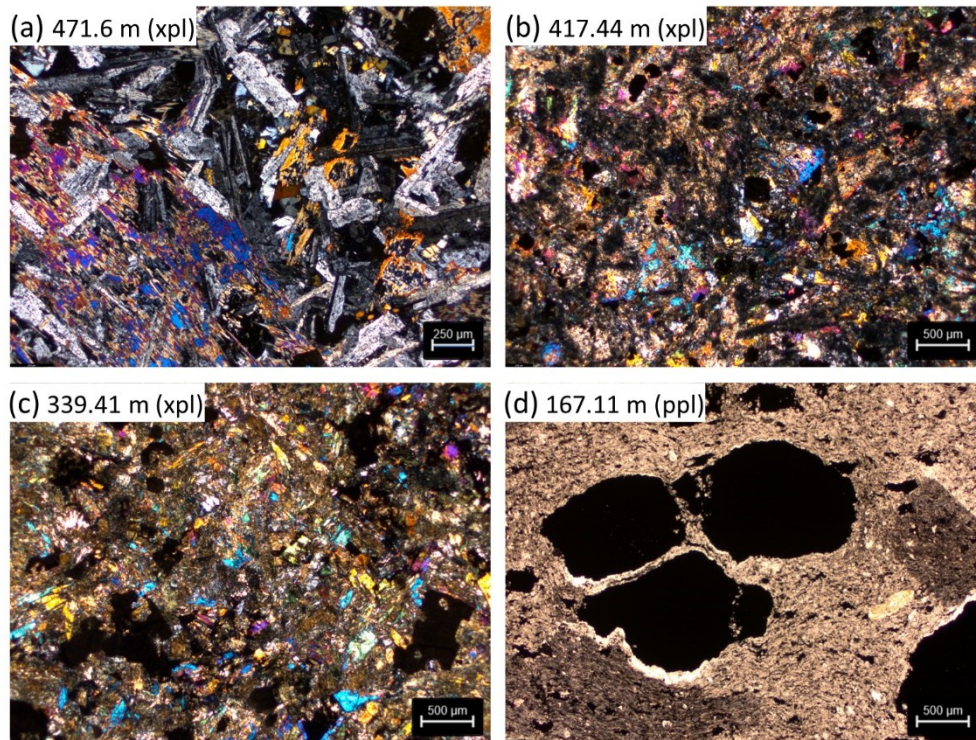
Figure 2: Photomicrographs of selected hand samples. (a) Weakly altered interior of the lower igneous body. Plagioclase (elongated grains with low birefringence) is preserved, pyroxene (medium birefringence poikilitic grains around plagioclase) is partly altered to phyllosilicates, including sericite and chlorite (fine-grained material in the bottom-left corner of the image). (b) Strongly altered upper part of the lower igneous body. Plagioclase is completely replaced and pyroxene is mostly replaced by secondary phyllosilicates. (c) Highly altered middle igneous body, similar to (b). In all three images (a-c), the blocky, nearly opaque grains are sphene, reflecting retention of Ti during alteration. (d) Tar balls (black rounded particles with low relief) within silty, calcareous shale. The shale matrix is itself fragmented (darker and lighter patches). The scale bar (bottom right corner in each image) is 250 µm in (a) and 500 µm in (b), (c) and (d). Xpl = crossed polars, ppl = plane-polarized light.
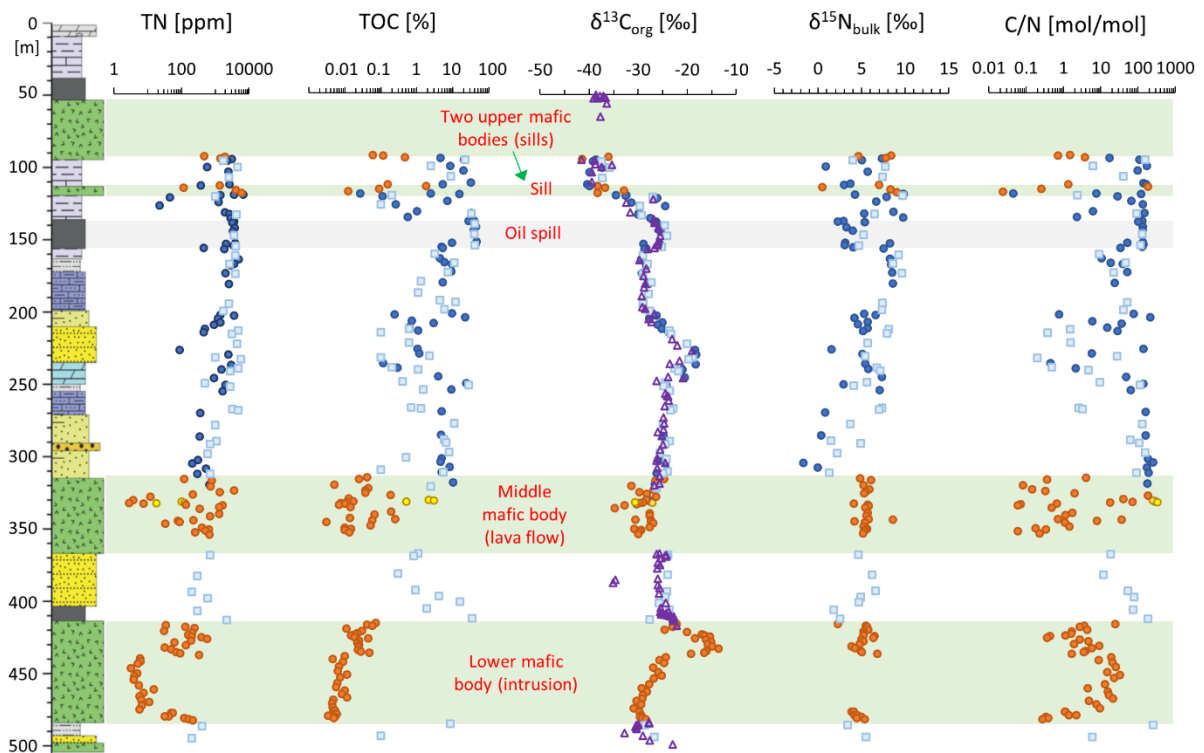
Figure 3: Stratigraphic patterns of total nitrogen (TN), total organic carbon (TOC), organic carbon isotopes, bulk nitrogen isotopes and molar C/N ratios. Orange circles = igneous bodies from this study, yellow circles = organic-rich veins within mafic rock, dark blue circles = sedimentary rocks from this study, light blue squares = sedimentary rocks from Kump *et al.* (2011), purple triangles = sedimentary rocks from Qu *et al.* (2012). Light green bands highlight data from the lower, middle and upper mafic bodies.
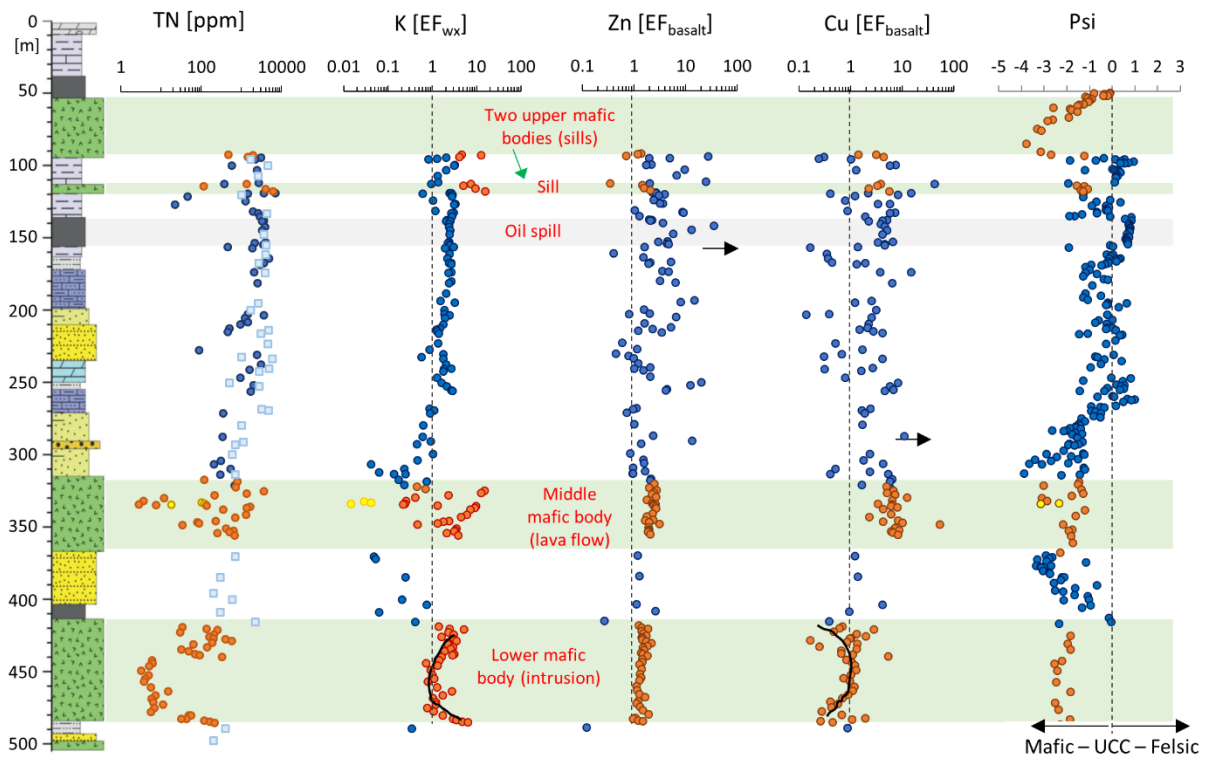
Figure 4: Stratigraphic patterns of total nitrogen (TN, same as in Fig. 2), potassium enrichment factors, accounting for weathering effects (K [EF_{wx}]), zinc (Zn) and copper (Cu) enrichment factors relative to basalt (EF_{basalt}), the provenance index Psi (see text for details). Some additional K data are taken from Kump *et al.* (2011). The vertical dashed lines in the Psi plot indicate the average value for upper continental crust UCC). Black lines in the K and Cu plots highlight enrichments and depletions, respectively, in the mafic intrusive body due to fluid alteration. The small black arrows in the Zn and Cu plots indicate positions of outliers with higher enrichments that are not shown on the graph. Zn and Cu abundances are normalized to average oceanic crust (White & Klein, 2014). Light green bands highlight data from the lower, middle and upper mafic bodies.

21
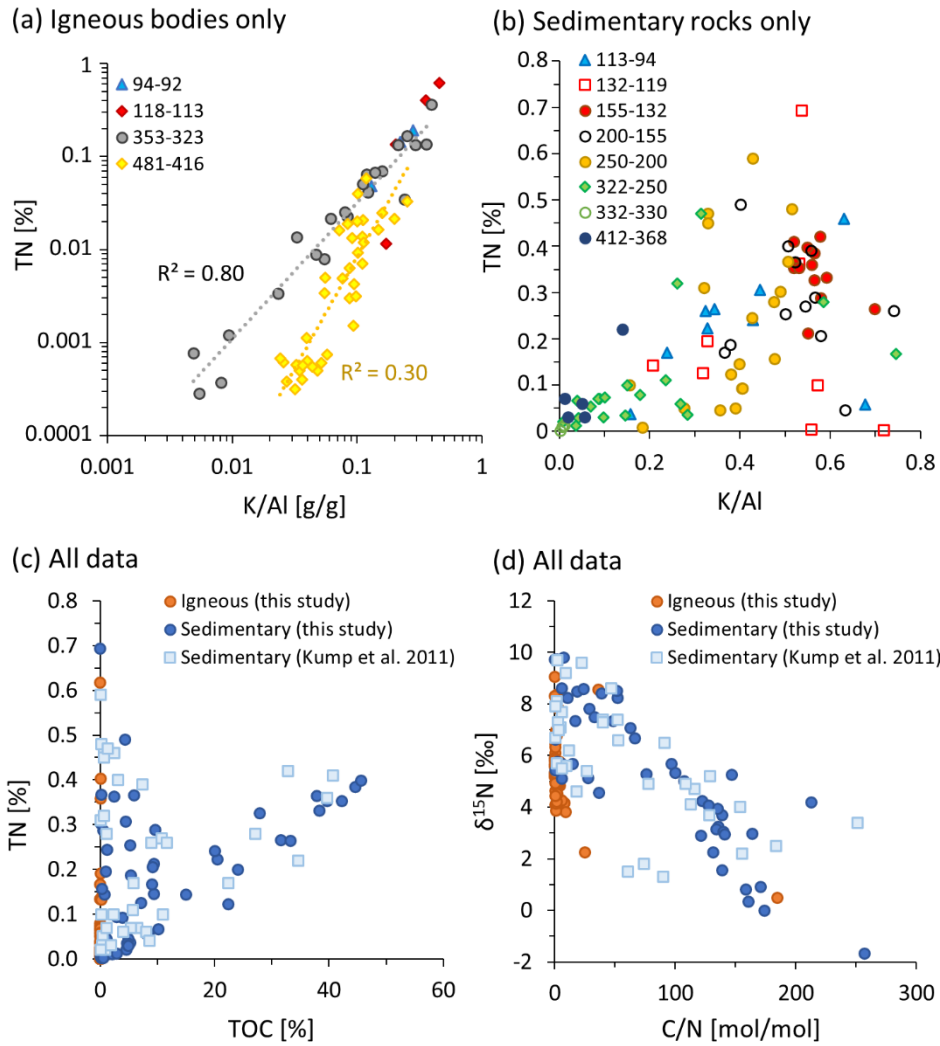
Figure 5: Scatter plots of total nitrogen versus potassium/aluminium ratios for igneous rocks (a), total nitrogen versus potassium/aluminium ratios for sedimentary rocks (b), total nitrogen versus total organic carbon (c), and bulk nitrogen isotopes versus molar C/N ratios (d). Panels (c) and (d) include all data from both igneous and sedimentary strata, following the same colour code as in Fig. 2. In panels (a) and (b), data are separated by stratigraphic depth.
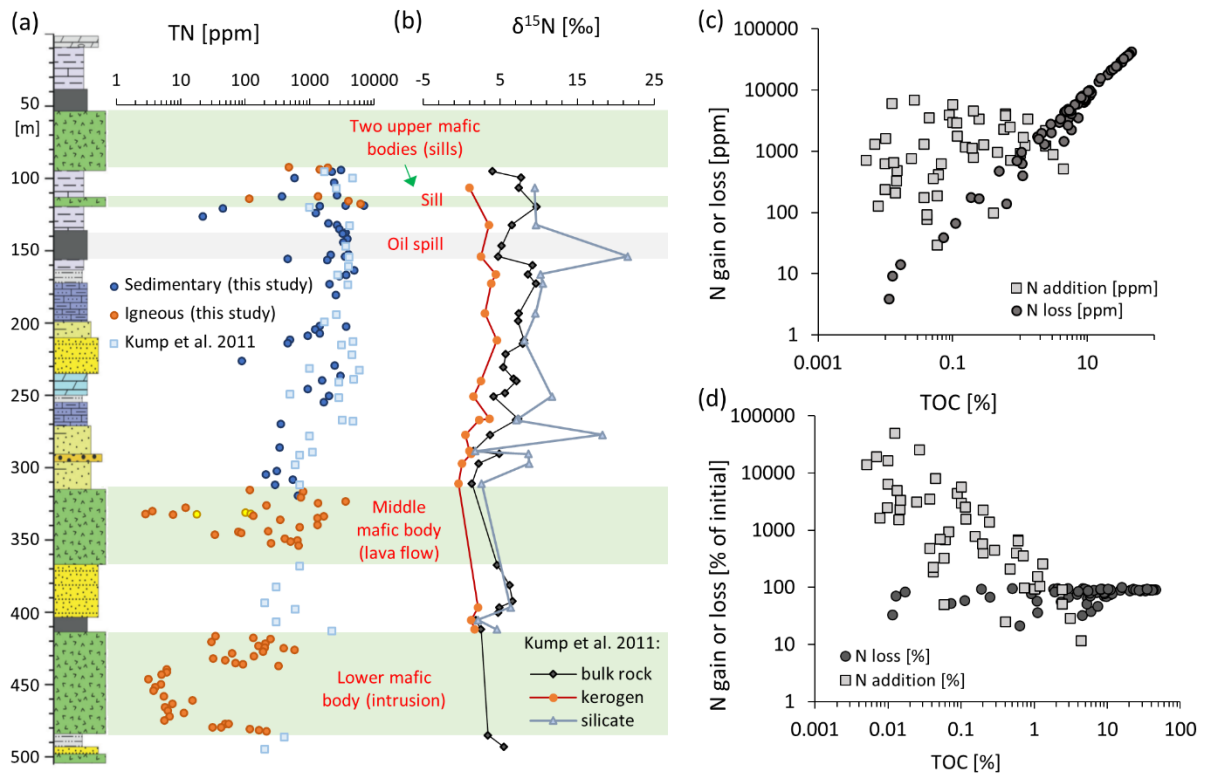
Figure 6: (a) Total nitrogen along the core. (b) Nitrogen isotopes for differing phases (Kump *et al.*, 2011). The silicate data were calculated by mass balance from the measured data for kerogen extracts and bulk rock. Relative abundances of organic- and silicate-bound N are highly variable along the core without particular stratigraphic trends and are therefore not plotted. (c) Nitrogen loss and gain (both expressed as positive numbers) for all samples, calculated from measured TOC and TN abundances and an assumed C/N starting value of 10. (d) Same as (c) but plotted in percent relative to the initial abundance of nitrogen in the given sample. Light green bands highlight data from the lower, middle and upper mafic bodies.
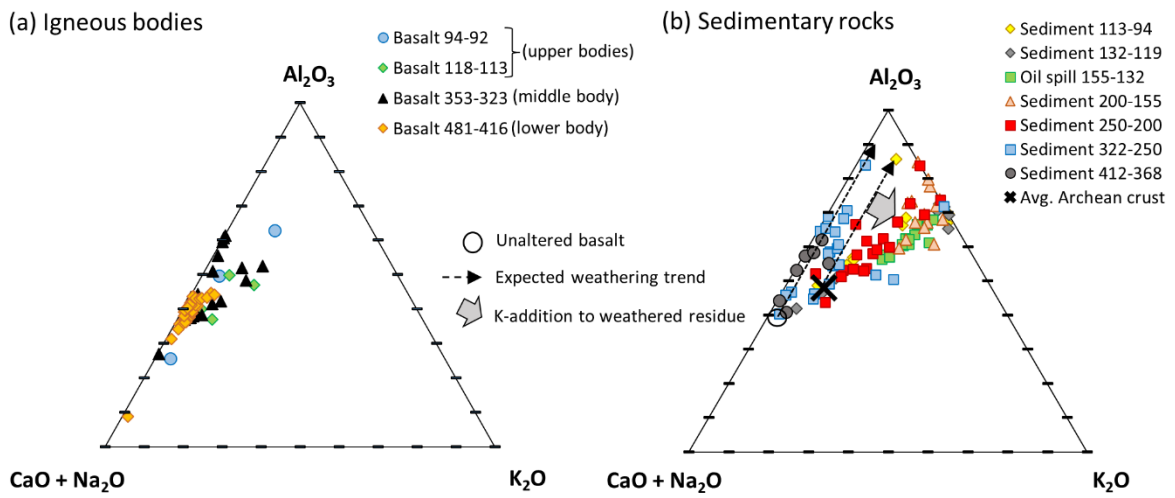
Figure 7: Ternary diagrams for igneous bodies (a) and for sedimentary rocks (b). Average Archean crust and expected alteration trends are taken from Fedo *et al.* (1995). The sedimentary rocks are corrected for Ca-contributions by calcite and phosphate following the procedure of Medaris *et al.* (2015).

References

Ader M, Cartigny P, Boudou J-P, Oh J-H, Petit E, Javoy M (2006) Nitrogen isotopic evolution of carbonaceous matter during metamorphism: methodology and preliminary results. *Chemical Geology,* **232**, 152-169.

Bauer A, Rooney AD, Lepland A (2020) Os and Nd isotope constraints on Paleoproterozoic global events as recorded in sediments from Russian Fennoscandia. *AGU Fall Meeting Abstracts*, PP020-003.

Blättler CL, Claire MW, Prave AR, Kirsimäe K, Higgins JA, Medvedev PV, Romashkin AE, Rychanchik DV, Zerkle AL, Paiste K, Kreitsmann T (2018) Two-billion-year-old evaporites capture Earth's great oxidation. *Science,* **360**, 320-323.

Boatman CD, Murray JW (1982) Modeling exchangeable NH_4^+ adsorption in marine sediments: Process and controls of adsorption. *Limnology and Oceanography,* **27**, 99-110.

Boudou JP, Schimmelmann A, Ader M, Mastalerz M, Sebilo M, Gengembre L (2008) Organic nitrogen chemistry during low-grade metamorphism. *Geochimica et Cosmochimica Acta,* **72**, 1199-1221.

Boudreau BP, Canfield DE (1988) A provisional diagenetic model for pH in anoxic porewaters: Application to the FOAM site. *Journal of Marine Research,* **46**, 429-455.

Bourbonnais A, Lehmann MF, Butterfield DA, Juniper SK (2012) Subseafloor nitrogen transformations in diffuse hydrothermal vent fluids of the Juan de Fuca Ridge evidenced by the isotopic composition of nitrate and ammonium. *Geochemistry, Geophysics, Geosystems,* **13**, doi: 10.1029/2011GC003863.

Brandes JA, Boctor NZ, Cody GD, Cooper BA, Hazen RM, Yoder Jr HS (1998) Abiotic nitrogen reduction on the early Earth. *Nature,* **395**, 365-367.

Brandes JA, Hazen RM, Yoder Jr HS (2008) Inorganic Nitrogen Reduction and Stability under Simulated Hydrothermal Conditions. *Astrobiology,* **8**, 1113-1126.

Brasier AT, Fallick AE, Prave AR, Melezhik VA, Lepland A, Scientists FD (2011) Coastal sabkha dolomites and calcitised sulphates preserving the Lomagundi-Jatuli carbon isotope signal. *Precambrian Research,* **189**, 193-211.

Brauhart CW, Huston DL, Groves DI, Mikucki EJ, Gardoll SJ (2001) Geochemical mass-transfer patterns as indicators of the architecture of a complete volcanic-hosted massive sulfide hydrothermal alteration system, Panorama district, Pilbara, Western Australia. *Economic Geology,* **96**, 1263-1278.

Brewer PG, Murray JW (1973) Carbon, nitrogen and phosphorus in the Black Sea. *Deep Sea Research and Oceanographic Abstracts* **20**, 803-818.

Brocks JJ, Jarrett AJ, Sirantoine E, Hallmann C, Hoshino Y, Liyanage T (2017) The rise of algae in Cryogenian oceans and the emergence of animals. *Nature,* **548**, 578-581.

Busigny V, Bebout GE (2013) Nitrogen in the silicate Earth: Speciation and isotopic behavior during mineral–fluid interactions. *Elements,* **9**, 353-358.

Caetano M, Falcão M, Vale C, Bebianno MJ (1997) Tidal flushing of ammonium, iron and manganese from inter-tidal sediment pore waters. *Marine Chemistry,* **58**, 203-211.

Campbell BJ, Polson SW, Zeigler Allen L, Williamson SJ, Lee CK, Wommack KE, Cary SC (2013) Diffuse flow environments within basalt-and sediment-based hydrothermal vent ecosystems harbor specialized microbial communities. *Frontiers in Microbiology,* **4**, doi: 10.3389/fmicb.2013.00182.

Casciotti KL (2009) Inverse kinetic isotope fractionation during bacterial nitrite oxidation. *Geochimica et Cosmochimica Acta,* **73**, 2061-2076.

Coplen TB (2019) *Report of Stable Isotopic Composition: Reference Materials USGS61, USGS62, and USGS63,* United States Geological Survey, Resont Stable Isotope Laboratory.

Črne AE, Melezhik VA, Lepland A, Fallick AE, Prave AR, Brasier AT (2014) Petrography and geochemistry of carbonate rocks of the Paleoproterozoic Zaonega Formation, Russia: Documentation of 13C-depleted non-primary calcite. *Precambrian Research,* **240**, 79-93.

Črne AE, Melezhik VA, Prave AR, Lepland A, Romashkin AE, Rychanchik DV, Hanski EJ, Luo Z (2013) Zaonega Formation: FAR-DEEP holes 12A and 12B, and neighbouring quarries. In: *Reading the Archive of Earth's Oxygenation: Volume 2: The Core Archive of the Fennoscandian Arctic Russia - Drilling Early Earth Project* (eds Melezhik VA, Prave AR, Fallick AE, Hanski EJ, Lepland A, Kump LR, Strauss H). Springer*,* pp. 946-1007.

Ehlmann BL, Mustard JF, Murchie SL (2010) Geologic setting of serpentine deposits on Mars. *Geophysical Research Letters,* **37**, DOI: 10.1029/2010GL042596.

Emerson S, Hedges J (1988) Processes controlling the organic carbon content of open ocean sediments. *Paleoceanography,* **3**, 621-634.

Engström P, Dalsgaard T, Hulth S, Aller RC (2005) Anaerobic ammonium oxidation by nitrite (anammox): implications for N2 production in coastal marine sediments. *Geochimica et Cosmochimica Acta,* **69**, 2057-2065.

Falkowski PG, Katz ME, Knoll AH, Quigg A, Raven JA, Schofield O, Taylor FJR (2004) The evolution of modern eukaryotic phytoplankton. *Science,* **305**, 354-360.

Fedo CM, Nesbitt HW, Young GM (1995) Unraveling the effects of potassium metasomatism in sedimentary rocks and paleosols, with implications for paleoweathering conditions and provenance. *Geology,* **23**, 921-924.

Filippov MM (1994) Current views on the organic precursor of shungite rocks. In: *The Organic Matter of Karelian Shungite Rocks (Genesis, Evolution and the Methods of Study)* (ed Filippov MM). Karelian Research Centre, Russian Academy of Sciences, Petrozavodsk*,* pp. 16-24 (in Russian).

Godfrey LV, Glass JB (2011) The geochemical record of the ancient nitrogen cycle, nitrogen isotopes, and metal cofactors. *Methods in Enzymology,* **486**, 483-506.

Godfrey LV, Poulton SW, Bebout GE, Fralick PW (2013) Stability of the nitrogen cycle during development of sulfidic water in the redox-stratified late Paleoproterozoic ocean. *Geology,* **41**, 655-658.

Hannah JL, Stein HJ, Zimmerman A, Yang G, Melezhik VA, Filippov MM, Turgeon SC, Creaser RA (2008a) Re-Os geochronology of shungite: A 2.05 Ga fossil oil field in Karelia. *Geochimica et Cosmochimica Acta,* **72**, A351.

Hannah JL, Stein HJ, Zimmerman A, Yang G, Melezhik VA, Filippov MM, Turgeon SC, Creaser RA (2008b) Re-Os geochronology of shungite: a 2.05 Ga fossil oil field in Karelia. *Geochimica et Cosmochimica Acta* **72**, A351.

Hitzman MW, Selley D, Bull S (2010) Formation of sedimentary rock-hosted stratiform copper deposits through Earth history. *Economic Geology,* **105**, 627-639.

Hoch MP, Fogel ML, Kirchman DL (1992) Isotope fractionation associated with ammonium uptake by a marine bacterium. *Limnology and Oceanography,* **37**, 1447-1459.

Hou LJ, Liu M, Jiang HY, Xu SY, Ou DN, Liu QM, Zhang BL (2003) Ammonium adsorption by tidal flat surface sediments from the Yangtze Estuary. *Environmental Geology,* **45**, 72-78.

Jessen GL, Lichtschlag A, Ramette A, Pantoja S, Rossel PE, Schubert CJ, Struck U, Boetius A (2017) Hypoxia causes preservation of labile organic matter and changes seafloor microbial community composition (Black Sea). *Science Advances,* **3**, p.e1601897.

Johnson B, Goldblatt C (2015) The Nitrogen budget of Earth. *Earth-Science Reviews,* **148**, 150-173.

Kipp MA, Krissansen-Totton J, Catling D (2021) High burial efficiency is required to explain mass balance in Earth's early carbon cycle. *Global Biogeochemical Cycles*, doi: 10.1029/2020GB006707.

Kipp MA, Stüeken EE (2017) Biomass recycling and Earth's early phosphorus cycle. *Science Advances,* **3**, doi: 10.1126/sciadv.aao4795.

Kipp MA, Stüeken EE, Yun M, Bekker A, Buick R (2018) Pervasive aerobic nitrogen cycling in the surface ocean across the Paleoproterozoic Era. *Earth and Planetary Science Letters,* **500**, 117-126.

Kithome M, Paul JW, Lavkulich LM, Bomke AA (1999) Effect of pH on ammonium adsorption by natural Zeolite clinoptilolite. *Communications in Soil Science & Plant Analysis,* **30**, 1417-1430.

Koehler MC, Stüeken EE, Hillier S, Prave AR (2019) Limitation of fixed nitrogen and deepening of the carbonate-compensation depth through the Hirnantian at Dob's Linn, Scotland. *Palaeogeography, Palaeoclimatology, Palaeoecology,* **534**, doi: 10.1016/j.palaeo.2019.109321.

Koistinen T, Stephens MB, Bogatchev V, Nordgulen Ø, Wenneström M, Korhonen J (2001) Geological Map of the Fennoscandian Shield. Scale 1:2,000,000. In: *Geological Surveys of Finland, Norway and Sweden and the North-West Department of Natural Resources of Russia.*

Konhauser KO, Robbins LJ, Pecoits E, Peacock C, Kappler A, Lalonde SV (2015) The Archean nickel famine revisited. *Astrobiology,* **15**, 804-815.

Konovalov SK, Murray JW, Luther GW, Tebo BM (2006) Processes controlling the redox budget for the oxic/anoxic water column of the Black Sea. *Deep Sea Research Part II: Topical Studies in Oceanography,* **53**, 1817-1841.

Kump LR, Junium C, Arthur MA, Brasier A, Fallick A, Melezhik V, Lepland A, CČrne AE, Luo G (2011) Isotopic evidence for massive oxidation of organic matter following the Great Oxidation Event. *Science,* **334**, 1694-1696.

Lilley MD, Butterfield DA, Olson EJ, Lupton JE, Macko SA, McDuff RE (1993) Anomalous CH4 and NH4+ concentrations at an unsedimented mid-ocean-ridge hydrothermal system. *Nature,* **364**, 45-47.

Lipp AG, Shorttle O, Sperling E, Brocks JJ, Cole D, Crockford PW, Del Mouro L, Dewing K, Dornbos SQ, Emmings JF, Farrell UC (2021) The composition and weathering of the continents over geologic time. *Geochemical Perspective Letters,* **7**, 21-26.

Lipp AG, Shorttle O, Syvret F, Roberts GG (2020) Major element composition of sediments in terms of weathering and provenance: implications for crustal recycling. *Geochemistry, Geophysics, Geosystems,* **21**, doi: 10.1029/2019GC008758.

Lyons TW, Reinhard CT, Planavsky NJ (2014) The rise of oxygen in Earth's early ocean and atmosphere. *Nature,* **506**, 307-315.

Martin AP, Prave AR, Condon DJ, Lepland A, Fallick AE, Romashkin AE, Medvedev P, Rychanchik DV (2015) Multiple Paleoproterozoic carbon burial episodes and excursions. *Earth and Planetary Science Letters,* **424**, 226-236.

Martin W, Baross J, Kelley D, Russell MJ (2008) Hydrothermal vents and the origin of life. *Nature Reviews Microbiology,* **6**, 805-814.

Medaris Jr LG, Boerboom TJ, Jicha BR, Singer BS (2015) Metasaprolite in the McGrath Gneiss, Minnesota, USA: viewing Paleoproterozoic weathering through a veil of metamorphism and metasomatism. *Precambrian Research,* **257**, 83-93.

Melezhik VA, Fallick AE, Filippov MM, Larsen O (1999) Karelian shungite—an indication of 2.0-Ga-old metamorphosed oil-shale and generation of petroleum: geology, lithology and geochemistry. *Earth-Science Reviews,* **47**, 1-40.

Paganini L, Villanueva GL, Roth L, Mandell AM, Hurford TA, Retherford KD, Mumma MJ (2020) A measurement of water vapour amid a largely quiescent environment on Europa. *Nature Astronomy,* **4**, 266-272.

Paiste K, Pellerin A, Zerkle AL, Kirsimäe K, Prave AR, Romashkin AE, Lepland A (2020) The pyrite multiple sulfur isotope record of the 1.98 Ga Zaonega Formation: Evidence for biogeochemical sulfur cycling in a semi-restricted basin. *Earth and Planetary Science Letters,* **534**, doi: 10.1016/j.epsl.2020.116092.

Prave AR, Kirsimäe K, Lepland A, Fallick AE, Kreitsmann T, Deines YE, Romashkin AE, Rychanchik DV, Medvedev PV, Moussavou M, Bakakas K (2021) The grandest of them all: the Lomagundi-Jatuli Event and Earth's oxygenation. *Journal of the Geological Society*, doi: 10.1144/jgs2021-1036.

Preiner M, Xavier J, Sousa F, Zimorski V, Neubeck A, Lang S, Greenwell H, Kleinermanns K, Tüysüz H, McCollom T, Holm N (2018) Serpentinization: Connecting Geochemistry, Ancient Metabolism and Industrial Hydrogenation. *Life,* **8**, doi: 10.3390/life8040041.

Priyatkina N, Khudoley AK, Ustinov VN, Kullerud K (2014) 1.92 Ga kimberlitic rocks from Kimozero, NW Russia: Their geochemistry, tectonic setting and unusual field occurrence. *Precambrian Research,* **249**, 162-179.

Puchtel IS, Arndt NT, Hofmann AW, Haase KM, Kröner A, Kulikov VS, Kulikova VV, Garbe-Schönberg CD, Nemchin AA (1998) Petrology of mafic lavas within the Onega plateau, central Karelia: evidence for 2.0 Ga plume-related continental crustal growth in the Baltic Shield. *Contributions to Mineralogy and Petrology,* **130**, 134-153.

Puchtel IS, Brügmann GE, Hofmann AW (1999) Precise Re–Os mineral isochron and Pb–Nd–Os isotope systematics of a mafic–ultramafic sill in the 2.0 Ga Onega plateau (Baltic Shield). *Earth and Planetary Science Letters,* **170**, 447-461.

Qu Y, Črne AE, Lepland A, Van Zuilen MA (2012) Methanotrophy in a Paleoproterozoic oil field ecosystem, Zaonega Formation, Karelia, Russia. *Geobiology,* **10**, 467-478.

Qu Y, van Zuilen MA, Lepland A (2020) Hydrothermal circulation and oil migration at the root of the heterogeneous micro-structure of carbonaceous material in the 2.0 Ga Zaonega Formation, Onega Basin, Russia. *Precambrian Research,* **343**, doi: 10.1016/j.precamres.2020.105705.

Rasmussen B, Muhling JR, Suvorova A, Fischer WW (2021) Apatite nanoparticles in 3.46–2.46 Ga iron formations: Evidence for phosphorus-rich hydrothermal plumes on early Earth. *Geology,* **49**, 647-651.

Robb L (2005) Introduction to ore-forming processes. In: *Wiley Blackwell*.

Rosenfeld JK (1979) Ammonium adsorption in nearshore anoxic sediments. *Limnology and Oceanography,* **24**, 356-364.

Roth L, Saur J, Retherford KD, Strobel DF, Feldman PD, McGrath MA, Nimmo F (2014) Transient water vapor at Europa's south pole. *Science,* **343**, 171-174.

Sánchez-Baracaldo P, Bianchini G, Wilson JD, Knoll AH (2021) Cyanobacteria and biogeochemical cycles through Earth history. *Trends in Microbiology*, doi: 10.1016/j.tim.2021.1005.1008.

Sander SG, Koschinsky A (2011) Metal flux from hydrothermal vents increased by organic complexation. *Nature Geoscience,* **4**, 145-150.

Schine CM, Alderkamp AC, van Dijken G, Gerringa LJ, Sergi S, Laan P, van Haren H, van de Poll WH, Arrigo KR (2021) Massive Southern Ocean phytoplankton bloom fed by iron of possible hydrothermal origin. *Nature Communications,* **12**, 1-11.

Schroeder PA, McLain AA (1998) Illite-smectites and the influence of burial diagenesis on the geochemical cycling of nitrogen. *Clay Minerals,* **33**, 539-546.

Smirnov A, Hausner D, Laffers R, Strongin DR, Schoonen MA (2008) Abiotic ammonium formation in the presence of Ni-Fe metals and alloys and its implications for the Hadean nitrogen cycle. *Geochemical Transactions,* **9**, doi:10.1186/1467-4866-1189-1185.

Stepanova AV, Samsonov AV, Larionov AN (2014) The final episode of the Mid-Paleoproterozoic magmatism in the Onega Basin: data on dolerites in Zaonezhski peninsula. *Proceedings of the Karelian Research Centre of RAS,* **1**, 3-16.

Stüeken EE (2020) Hydrothermal vents and organic ligands sustained the Precambrian copper budget. *Geochemical Perspectives Letters,* **16**, 12-16.

Stüeken EE, Boocock TJ, Robinson, A., Mikhail S, Johnson BW (2021a) Hydrothermal recycling of sedimentary ammonium into oceanic crust and the Archean ocean at 3.24 Ga. *Geoloy*, doi:10.1130/G48844.48841.

Stüeken EE, de Castro M, Krotz L, Brodie C, Iammarino M, Giazzi G (2020) Optimized switch-over between CHNS abundance and CNS isotope ratio analyses by Elemental Analyzer-Isotope Ratio Mass Spectrometry: Application to six geological reference materials. *Rapid Communications in Mass Spectrometry*, doi: 10.1002/rcm.8821.

Stüeken EE, Gregory DD, Mukherjee I, McGoldrick P (2021b) Sedimentary exhalative venting of bioavailable nitrogen into the early ocean. *Earth and Planetary Science Letters,* **565**, doi: 10.1016/j.epsl.2021.116963.

Stüeken EE, Zaloumis J, Meixnerová J, Buick R (2017) Differential metamorphic effects on nitrogen isotopes in kerogen extracts and bulk rocks. *Geochimica et Cosmochimica Acta,* **217**, 80-94.

Swanner ED, Planavsky NJ, Lalonde SV, Robbins LJ, Bekker A, Rouxel OJ, Saito MA, Kappler A, Mojzsis SJ, Konhauser KO (2014) Cobalt and marine redox evolution. *Earth and Planetary Science Letters,* **390**, 253-263.

van Raaphorst W, Malschaert JF (1996) Ammonium adsorption in superficial North Sea sediments. *Continental Shelf Research,* **16**, 1415-1435.

Viviano CE, Moersch JE, McSween HY (2013) Implications for early hydrothermal environments on Mars through the spectral evidence for carbonation and chloritization reactions in the Nili Fossae region. *Journal of Geophysical Research: Planets,* **118**, 1858-1872.

Waite JH, Combi MR, Ip WH, Cravens TE, McNutt RL, Kasprzak W, Yelle R, Luhmann J, Niemann H, Gell D, Magee B (2006) Cassini ion and neutral mass spectrometer: Enceladus plume composition and structure. *Science,* **311**, 1419-1422.

White WM, Klein EM (2014) Composition of the Oceanic Crust. *Treatise on Geochemistry,* **4**, 457-496.

Williams LB, Ferrell Jr RE, Chinn EW, Sassen R (1989) Fixed-ammonium in clays associated with crude oils. *Applied Geochemistry,* **4**, 605-616.

Williams LB, Ferrell RE (1991) Ammonium substitution in illite during maturation of organic matter. *Clays and Clay Minerals,* **39**, 400-408.

Williams LB, Wilcoxon BR, Ferrell RE, Sassen R (1992) Diagenesis of ammonium during hydrocarbon maturation and migration, Wilcox Group, Louisiana, USA. *Applied Geochemistry,* **7**, 123-134.

Yen AS, Morris RV, Ming DW, Schwenzer SP, Sutter B, Vaniman DT, Treiman AH, Gellert R, Achilles CN, Berger JA, Blake DF (2021) Formation of tridymite and evidence for a hydrothermal history at gale crater, Mars. *Journal of Geophysical Research: Planets,* **126**, p.e2020JE006569.